nature communications

Article

https://doi.org/10.1038/s41467-025-65539-9

Polymer-constrained excimer enables flexible and self-healable optoelectronic elastomer for mechanical sensor

Received: 7 May 2025

Accepted: 17 October 2025

Published online: 25 November 2025

Check for updates

Shuyu Zheng[1,2], Dazhe Zhao[3], Nengjie Cao[1], Jiajia Zhou[1,2] ✉, Junwen Zhong[3] ✉ & Haobing Wang[1,2] ✉

The development of high-performance, flexible, and self-healable optoelectronic materials is pivotal for advancing next-generation wearable technologies. In this study, we introduce nanoscale naphthyl-naphthyl microphase separation into a polyisoprene matrix, endowing olefin copolymers with exceptional mechanical properties, high flexibility, and intrinsic self-healing capabilities at room temperature without external stimuli. Notably, by employing a "polymer-constrained excimer" strategy, these copolymers exhibit remarkable photoluminescent properties, achieving an ultra-high photoluminescence quantum yield (PLQY > 98%) through the formation of naphthyl-naphthyl excimers. Experimental and theoretical analyses reveal that under the encapsulation of flexible *cis*-1,4-polyisoprene segments, nanoscale naphthyl aggregates form stable excimers upon UV stimulation, resulting in extraordinary fluorescence quantum efficiency. Additionally, the nanoscale aggregation of naphthyls imparts superior electret performance to these copolymers, making them ideal for opto-electro-mechanical sensors for the robotic hand and other devices.

The demand for high-performance, flexible, and self-healing optoelectronic materials has surged with the rise of next-generation wearable technologies, such as electronic skin, smart sensors, and humanoid robots[1–11]. These applications require materials that are lightweight, durable, and capable of capturing, analyzing, and conveying multidimensional signals (e.g., optical and electrical) while providing high-precision feedback[12–14]. However, traditional high-performance materials often suffer from high rigidity or require good dispersion in non-functional matrices, compromising their efficiency and durability in wearable devices. Thus, developing materials that combine mechanical flexibility, intrinsic self-healing properties, and high optical/electronic sensitivity remains a significant challenge[15,16].

Polyolefin thermoplastic elastomers (TPEs), known for their low density, cost-effectiveness, flexibility, and potential for self-healing, offer a promising platform for wearable integration[17–25]. For instance, Hou et al. recently demonstrated that homopolymerization of isoprene by rare-earth catalyst could yield sequence-controlled polyisoprenes with microphase-separated nanodomains of short 3,4-polyisoprene blocks (hard segments) within a flexible *cis*-1,4-polyisoprene matrix (soft segments), exhibiting excellent elasticity and self-healability[26]. However, the limited optical and electronic functionality of non-polar polyolefins restricts their application in optoelectronic devices. To address this, incorporating functional moieties into polyolefin matrices has been explored[27–31], but achieving high

[1]Advanced Institute for Soft Matter Science and Technology (AISMST), School of Emergent Soft Matter, State Key Laboratory of Pulp and Paper Engineering, South China University of Technology, Guangzhou, China. [2]Guangdong Provincial Key Laboratory of Functional and Intelligent Hybrid Materials and Devices, Guangdong Basic Research Center of Excellence for Energy and Information Polymer Materials, South China University of Technology, Guangzhou, China. [3]Department of Electromechanical Engineering and Centre for Artificial Intelligence and Robotics, University of Macau, Macau SAR, China.
✉e-mail: zhouj2@scut.edu.cn; junwenzhong@um.edu.mo; haobingwang@scut.edu.cn

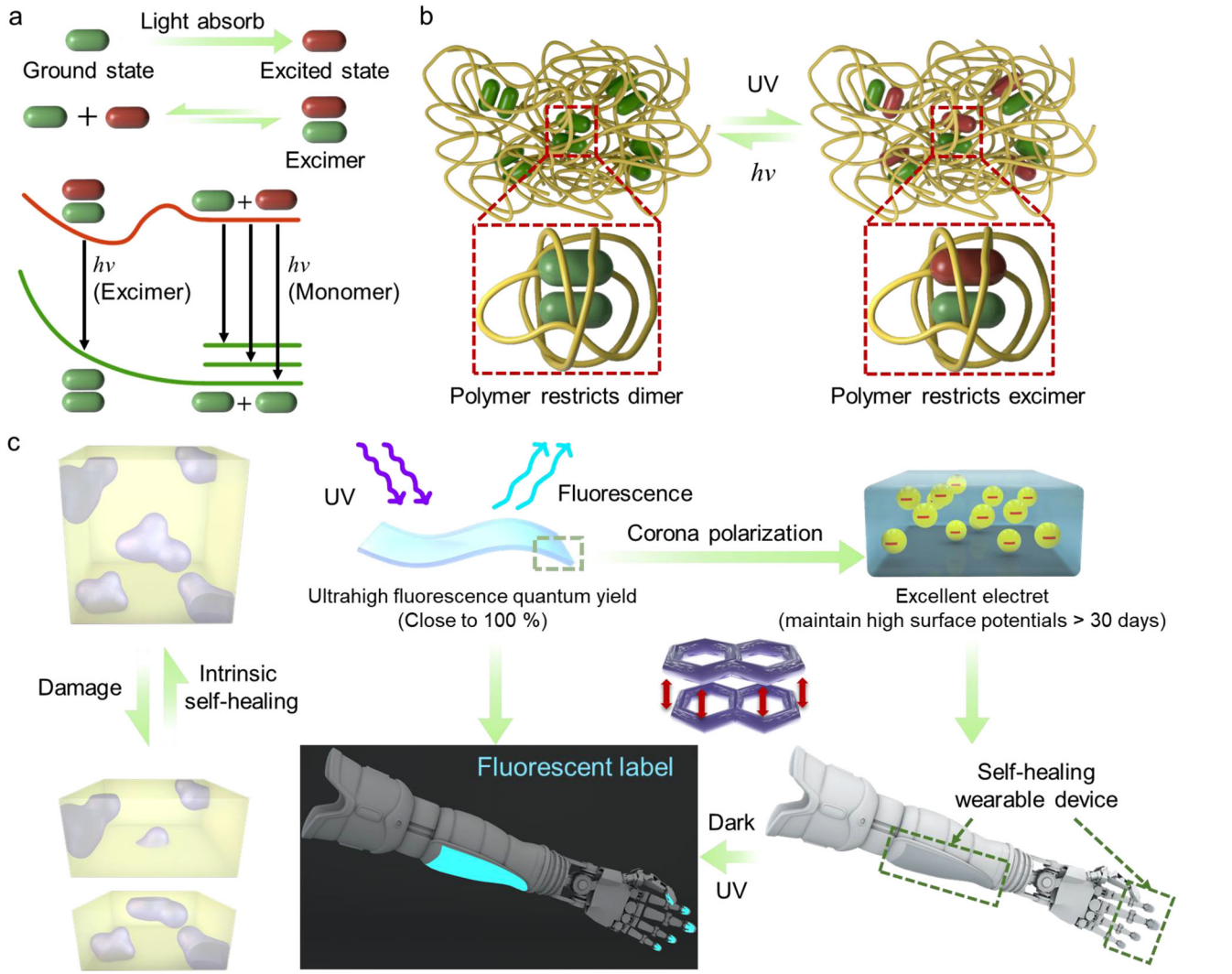

Fig. 1 | Molecular design and multifunctional integration of isoprene-*co*-1-vinylnaphthalene copolymers. a *Mechanism of excimer formation*: The π-π stacking interaction between adjacent naphthalene groups enables the formation of excited-state dimers (excimers), leading to red-shifted fluorescence emission compared to monomeric chromophores. **b** *The "polymer-restricted excimer" strategy*: By precisely controlling the spacing and mobility of naphthalene side chains through copolymer architecture, the excimer formation is confined within the polymer matrix. **c** *Integration of multifunctional properties*: The copolymer system simultaneously achieves (i) *self-healing* via reversible physical crosslinking, (ii) *high fluorescence efficiency* due to optimized excimer emission, and (iii) *electret behavior* through charge trapping at the naphthalene-rich microdomains.

photoluminescence efficiency alongside self-healing properties remains elusive.

Introducing aromatic chromophores into polymer backbones can enhance optoelectronic functionality[32–37], which is valuable for optical sensing, biomedical imaging, and energy conversion[38–42]. Precise control of intermolecular spacing of aromatic units is critical, as excessive overlap can lead to aggregation-caused quenching (ACQ)[43–46]. Conversely, appropriate aromatic-aromatic interactions may also facilitate excimer formation[47–51], thereby enhancing fluorescence quantum yields of materials (Fig. 1a). However, traditional excimer formation typically requires rigid scaffolds or solvent dispersion[52–56], limiting its application in flexible wearable materials.

Aromatic-containing polymers also constitute an important category of polymer electrets. These materials exhibit a distinctive characteristic that sets them apart from most alternatives: the innate capacity to produce stable electrostatic charges through mechanical stimulation (e.g., vibration, compression) in the absence of external polarization fields[57]. This unique attribute makes them particularly valuable for applications ranging from acoustic transducers to mechanical energy harvesting systems. Beyond their electret properties, these polymers offer additional advantages including intrinsic flexibility, robust mechanical durability, and excellent compatibility with organic and soft polymeric substrates-features that clearly differentiate them from conventional inorganic electret materials. Such exceptional properties have generated growing research interest in their application for next-generation flexible electronic devices, including conformal electromechanical sensors, epidermal electronic systems, and tactile feedback interfaces[58–62]. Nevertheless, significant challenges persist in developing intrinsically compliant electret materials. Notably, the integration of advanced functional characteristics - especially self-healing mechanisms to improve service lifetime - represents an entirely unexplored research frontier in soft electret technology.

In this study, we synthesize a family of 1-vinylnaphthalene and isoprene copolymers with varying microstructures and sequences. By employing the formation of nanoscale naphthyl-naphthyl microphase separation in a polyisoprene matrix, these copolymers exhibit a rare combination of mechanical robustness and intrinsic self-healing capabilities at room temperature without external stimuli. The polyisoprene segments constrain naphthyl-naphthyl nanophases, enabling

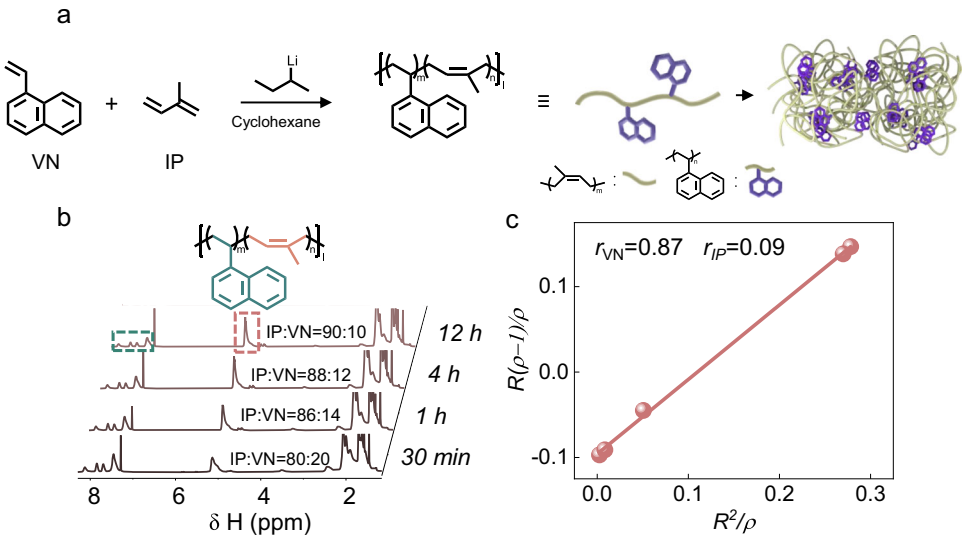

Fig. 2 | Synthesis of VN-*co*-IP (PNI). a Copolymerization of IP and VN. **b** ^{1}H NMR spectra tracking copolymerization of IP and VN ($CDCl_3$, 400 MHz). **c** Reactivity ratio plot for IP and VN during copolymerization.

the formation of stable excimers (Fig. 1b). Under UV stimulation, this "polymer-constrained excimer" strategy enables the copolymer with an ultra-high photoluminescence quantum yield (PLQY > 98%) in the solid state. Furthermore, the naphthyl-naphthyl nanophase demonstrates exceptional electret performance with over 30-day charge retention, expanding its potential applications in self-healable opto-electro-mechanical sensing for the robotic hand (Fig. 1c).

Results

Synthesis of copolymers

The copolymerization of isoprene (IP) with vinyl monomers such as styrene (St) and 1-vinylnaphthalene (VN) was initiated by *sec*-butyllithium (*s*-BuLi) in cyclohexane (Fig. 2a, Supplementary Figs. 1, 2). For IP: St (feed ratio 90: 10), tapered block copolymers formed, with IP**:** St ratios of 98: 2, 98: 2, 96: 4, and 90: 10 at 30 min, 1 h, 4 h, and 12 h, respectively[63]. In contrast, real-time monitoring of IP/VN copolymerization (feed ratio 90: 10) revealed simultaneous incorporation of both monomers, with IP: VN ratios of 80: 20, 86: 14, 88: 12, and 90: 10 at the same time, suggesting a random copolymerization (Fig. 2b). The reactivity ratios of this copolymerization were calculated as $r_{IP} = 0.09$ and $r_{VN} = 0.87$, which further confirmed that the copolymerization took place in a random fashion (Fig. 2c). As the [IP]/[VN] feed ratio was decreased from 90/10 to 80/20, 75/25, 70/30, 65/35, 60/40, 50/50, and 30/70, the [IP]/[VN] ratio of the resulting copolymers showed a similar trend from 90/10 to 30/70, respectively (Supplementary Table 1 and Figs. 3, 4). The ^{13}C NMR and DOSY NMR spectra in $CDCl_3$ demonstrated the formation of the random copolymer of poly-(1-vinylnaphthalene)-*random*-(*cis*-1,4-isoprene) (PNI) rather than the mixture of two homopolymers (Supplementary Figs. 5, 6).

Mechanical and self-healing properties of PNI copolymer

The VN-*co*-IP copolymer (PNI) with 10 mol% VN content exhibited a glass-transition temperature (T_g) at −45 °C (Fig. 3a and Supplementary Fig. 7). As the VN content increased from 10 mol% to 70 mol%, the copolymers showed incremental glass-transition temperatures (T_g) from −45 °C to −30 °C, 10 °C, 40 °C, 70 °C, and 100 °C (Fig. 3a), respectively. These copolymers with different VN contents showed distinct mechanical properties at room temperature. For instance, when the content of VN was lower than 20 mol%, the copolymer exhibited very weak tensile strength (<0.1 MPa) and poor elasticity. When the content of VN was higher than 40 mol%, the copolymers showed much higher T_g (Fig. 3a) and behaved like hard plastics with high Young's modulus (100 MPa) and tensile strength at break (25 MPa, Fig. 3b). The optimal copolymer with approximately 30 mol% VN content (T_g = 5 °C) showed typical features of the elastomer with Young's modulus of 0.5 ± 0.1 MPa, breaking strength of 1 ± 0.1 MPa, and elongation at break of 2020 ± 20% (Supplementary Table 2).

With the similar IP: VN ratios of approximately 70: 30, the higher molecular-weight copolymers (M_n = 117, 143, 184, 201, and 227 kDa, code as P1-P5, Table 1 and Supplementary Fig. 4) demonstrated the higher tensile strength (2.4 ± 0.1, 3 ± 0.5, 12 ± 0.5, 20 ± 1 and 25 ± 1 MPa) and excellent stretchability with elongations of 1200% to 1950% (Fig. 3c and Supplementary Table 2). In addition to excellent elasticity (Supplementary Fig. 8), these pristine copolymers showed remarkable self-healability. For instance, when a dog-bone-shaped film sample of P3 was completely cut by a razor blade, the material could be stretched to 550% after the cut area was contacted and gently pressed for less than 15 s at 25 °C in air, and then allowed to self-repair for 30 min (Fig. 3d). After healing for 48 h, the fracture healed almost completely as evidenced by observation of a comparable elongation with that of the pristine sample, its original tensile strength of 11 MPa with an elongation of 1270%. When the sample was cut, contacted, and placed under 36 °C (human body temperature) in air, a complete recovery was observed within 6 h, indicating its high potential for self-healing wearable devices or electronic skin (Supplementary Fig. 9c). The picture of a square hot-pressing P3 sheet (dumbbell-configured specimens according to JIS K-6251-7; width: 2 mm; length: 12 mm; thickness: 1 mm) and a movie of a tiny pocket made by P3 full of water are shown in Fig. 3e and Supplementary Movie 1 to present the self-healing effect visually. Tougher copolymers with higher molecular weight, such as P5, could also reach their original tensile strength of as high as 24.5 MPa with an elongation of 1200%, albeit with a longer healing time (7 days) at room temperature (Supplementary Fig. 9a).

When a film sample of P3 was cut by a razor blade, the crack became almost invisible within 1 min at room temperature in the air without any external intervention (Fig. 3f; see also Supplementary Movie 2), standing in sharp contrast with the VN ratios of 50 mol%, which presented no self-healability under the same conditions. As for PNI with 10 mol%, the sample showed limited self-healability and was not able to completely heal the wound in 30 min. A triblock copolymer of VN-*b*-IP-*b*-VN with a total VN content of 30 mol% (NIN-3) also showed no self-healability under the same conditions (Fig. 3f), demonstrating that the self-healing property of the copolymers significantly depends on their microstructures (Supplementary Figs. 10–14). We propose

https://doi.org/10.1038/s41467-025-65539-9

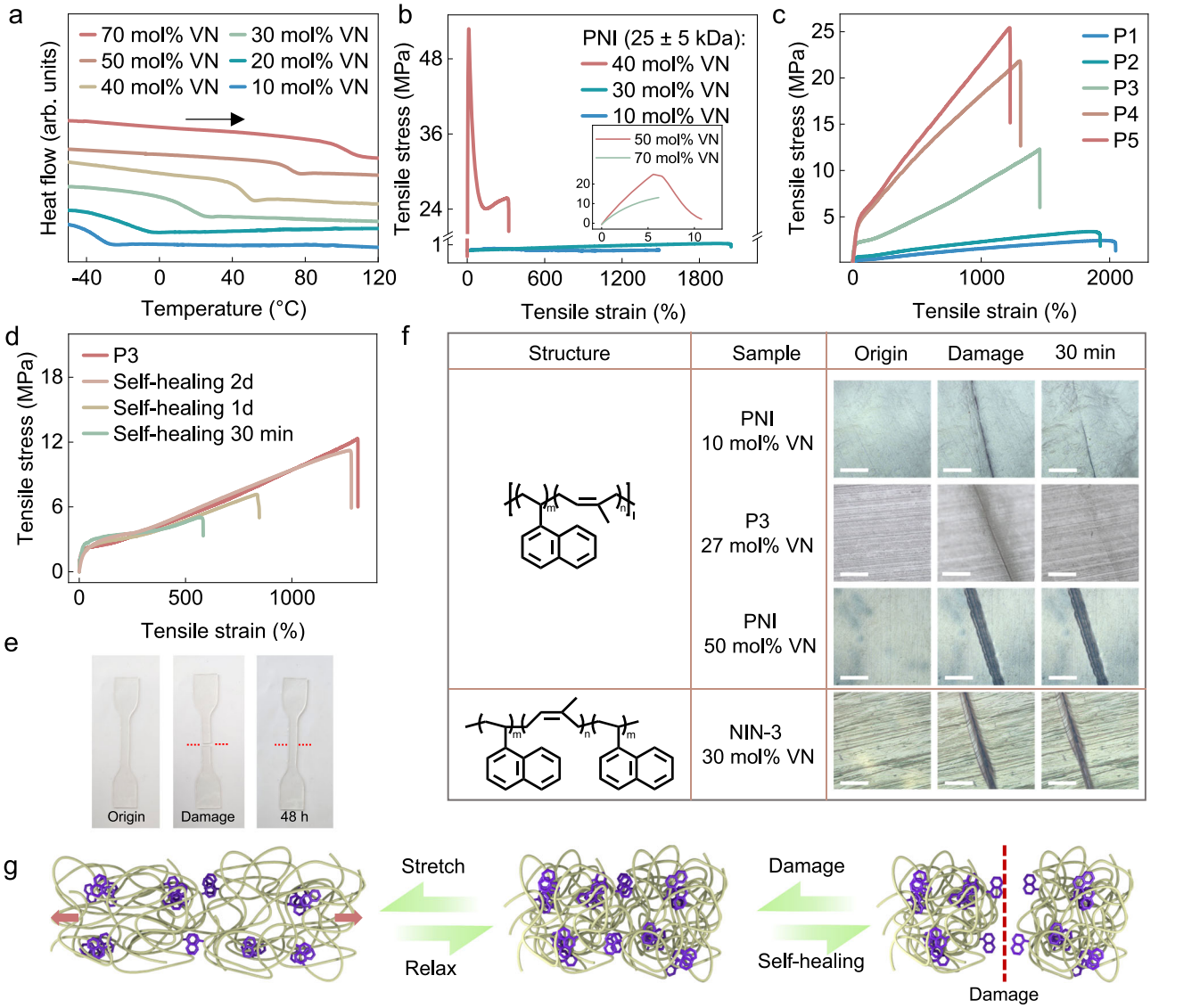

Fig. 3 | Mechanical and self-healing properties of VN-*co*-IP (PNI). a DSC analysis (use the data from the second heating, and the endothermic direction is from top to bottom) of PNI with varying VN content (10–70 mol%). **b** Stress-strain curves of PNI copolymer with different VN contents at low M_n (25 ± 5 kDa). **c** Stress-strain curves of P1-P5 (M_n = 117 to 227 kDa, IP/VN ratios = ~70/30). **d** Self-healing tests of P3. **e** P3 film with different states: original, completely severed, and fully self-healed after 48 h (dumbbell-configured specimens according to JIS K-6251-7; width: 2 mm; length: 12 mm; thickness: 1 mm). **f** Optical microscopy of healed PNI films (scale bar: 200 μm). **g** Proposed mechanism for the mechanical and self-healing properties of PNI copolymer.

that the microphase-separated naphthyl nanodomains act as cross-linking points within the flexible *cis*-1,4-polyisoprene matrix, thus enforcing elasticity and toughness (Fig. 3g). The exceptionally rapid self-healing may result from the high mobility of the *cis*-1,4-polyisoprene segments with low T_g, which could induce the rapid re-aggregation of the naphthyl groups through π-π interaction to repair the mechanical damage.

Optical property of PNI copolymer

P3 prepared by hot pressing demonstrated excellent optical transparency in the visible spectrum (400-800 nm), achieving transmittance values of 82-92% (Fig. 4a) due to its amorphous nature (Fig. 3a). Interestingly, under ultraviolet light irradiation, the colorless P3 sample exhibited excellent photoluminescent performance (Fig. 4b), demonstrating a fluorescence quantum efficiency >98% (Fig. 4c and Supplementary Fig. 15). In contrast, both naphthalene (Naph) dispersed in polyisoprene (30 mol%) and THF solution (1 M) didn't show any notable fluorescence performance (Fig. 4b). We investigated the fluorescence behavior during the self-healing process of P3 (Supplementary Fig. 16). Immediately after cutting and rejoining the P3 specimen, we observed a significant fluorescence enhancement. This phenomenon likely resulted from increased light absorption at the freshly exposed wound surfaces compared to intact regions, where excitation light was attenuated by the penetration process and thus generated less fluorescence. As self-healing progressed, the fluorescence intensity gradually decreased, eventually returning to near-baseline levels upon complete restoration of the material.

To investigate the fluorescence mechanism, we examined the fluorescence property of P3. With a concentration of 0.2 g/L P3 in THF, it exhibited a broad emission range of 310–500 nm with maximum peaks at 340 and 400 nm (Fig. 4d). In contrast, the solid P3 film exhibited a much stronger emission in the range of 340–500 nm with maximum peaks at 396 nm (Fig. 4e), possibly caused by the formation of naphthyl-naphthyl excimers in P3. To verify this hypothesis, the

https://doi.org/10.1038/s41467-025-65539-9

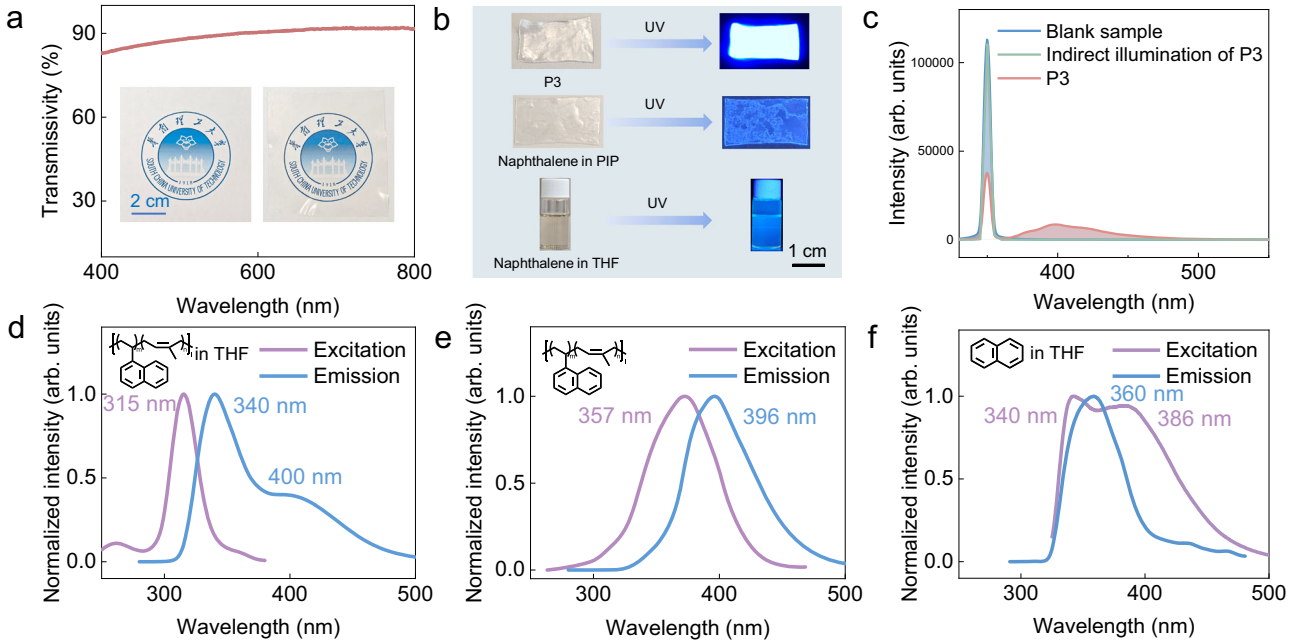

Fig. 4 | The optical properties of VN-*co*-IP (PNI). a Visible light transmittance spectrum of P3. **b** Photoluminescence under UV light: P3 (solid), Naph/PIP, Naph in THF (1 M). **c** PLQY measurement of P3. **d**–**f** Fluorescence spectra of: **d** P3 (THF, 0.2 g/L), **e** P3 (solid), **f** Naph in THF (1 M).

Table 1 | Copolymerization of isoprene (IP) and 1-vinylnaphthalene (VN)[a]

Code	[IP]: [VN]: [s-BuLi][b]	conv. IP (%)	conv. VN (%)	M_n (×10³ g mol⁻¹)[c]	IP/VN[d]	M_w/M_n[c]	T_g (°C)[e]
P1	1500: 600: 1	96%	82%	117	73/27	1.1	10
P2	1800: 720: 1	95%	82%	143	72/28	1.6	10
P3	2000: 800: 1	92%	79%	184	73/27	2.5	11
P4	2200: 880: 1	90%	78%	201	73/27	2.3	13
P5	2500: 1000: 1	90%	77%	227	73/27	2.3	15
P6	2500: 300: 1	90 %	83 %	201	90/10	1.5	−40
P7	800: 950: 1	77 %	65 %	86	50/50	3.6	70

[a]Conditions: Sec-Butyllithium (s-BuLi) (1.3×10^{-2} mmol); 50 mL Cyclohexane; Room temperature.
[b]Feed ratio (in moles) of isoprene (IP), 1-vinylnaphthalene (VN), and s-BuLi.
[c]Determined by gel permeation chromatography (GPC) in tetrahydrofuran (THF) at 35 °C against polystyrene standard. M_n = number-average molecular weight, M_w = weight-average molecular weight.
[d]Molar ratio of isoprene (IP) and 1-vinylnaphthalene (VN) in the copolymer, determined by ^{1}H nuclear magnetic resonance (NMR) analysis.
[e]Determined by differential scanning calorimetry (DSC).

fluorescence spectra of naphthalene in THF with different concentrations were recorded (Fig. 4f and Supplementary Fig. 17). The diluted Naph solution (1.0 mM) exhibited excitation in the range of 280–380 nm with maximum peaks at 307 nm and 359 nm and an emission in the range of 310–360 nm with a maximum peak at 330 nm (Supplementary Fig. 17a). Upon increasing the Naph concentration to 1.0 M, both excitation and emission showed a significant red shift in the range of 325–480 nm with maximum peaks at 340 nm and 386 nm and in the range of 320–480 nm with maximum peak at 360 nm, respectively (Fig. 4f), consistent with the optical behavior of Naph excimers in the solution state[47–49]. The fluorescence lifetime is also key evidence for the formation of excimers. When the concentration of Naph in THF increased from 1.0 mM to 1.0 M, the fluorescence lifetime increased from 0.47 ns to 1.11 ns. Remarkably, in comparison to the copolymer in solution (fluorescence lifetime: 1.11 ns), the fluorescence lifetime of P3 in the solid state significantly increased to 5.09 ns (Fig. 5a). The temperature-dependent fluorescence spectroscopy of P3 also showed a significant fluorescence intensity increase as the temperature decreased (Fig. 5b) due to the further reduction of non-radiative decay; these two phenomena further confirmed the existence of stable excimers in the solid state.

The VN content significantly impacted the fluorescence quantum yield of the copolymer. As the VN content increased from 10 mol% to 50 mol%, the fluorescence quantum efficiency of the copolymers initially increased from 45% (10 mol% VN), reached a peak at 98% (30 mol% VN) and then decreased to 18% (50 mol% VN) (Fig. 5c and Supplementary Fig. 18). The decrease in fluorescence quantum yield at low VN content (e.g., 10 mol%) may be attributed to a lower probability of excimer formation. In contrast, when the VN content was higher (e.g., 50 mol%), the aggregation of numerous naphthyl groups within the copolymer caused a phenomenon of aggregation-induced fluorescence quenching, which reduced the quantum yield of the copolymer. Additionally, the quantum yields of Naph with different molar ratios (10 mol% to 50 mol%) dispersed into the polyisoprene (PIP) were recorded, and all these samples showed low quantum yields (<3%). Notably, the fluorescent quantum yield of P3 in this study was significantly higher than that of reported fluorescent solid polymers (Fig. 5d).

https://doi.org/10.1038/s41467-025-65539-9

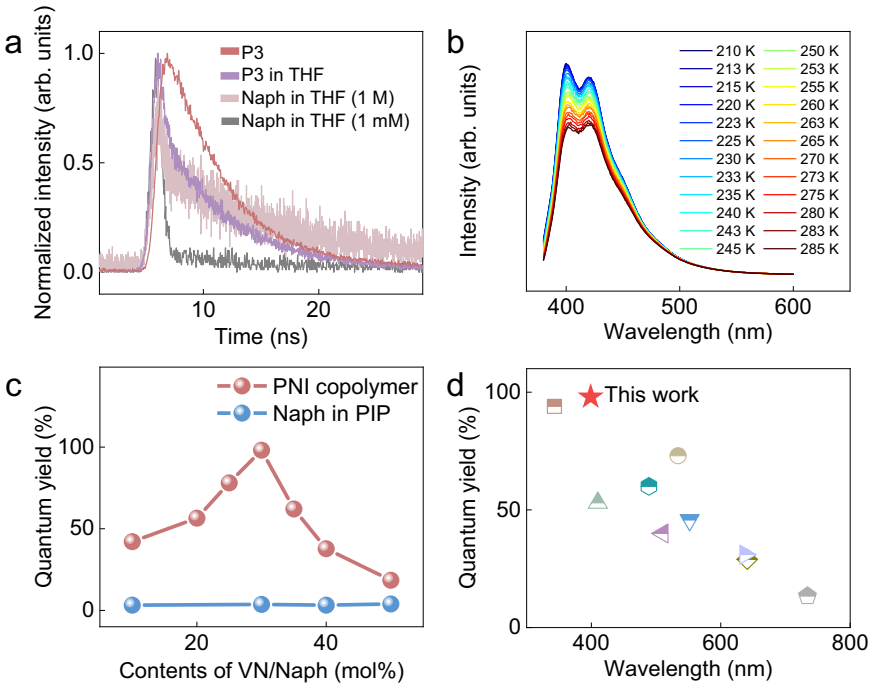

Fig. 5 | The optical properties of VN-*co*-IP (PNI). a Fluorescence lifetime analysis. **b** Temperature-dependent fluorescence spectroscopy of P3 (from 210 K to 285 K). **c** PLQY *vs.* VN/Naph content[67,68]. **d** Comparison with literature PLQY values of recent fluorescent polymers[25,34,69–75].

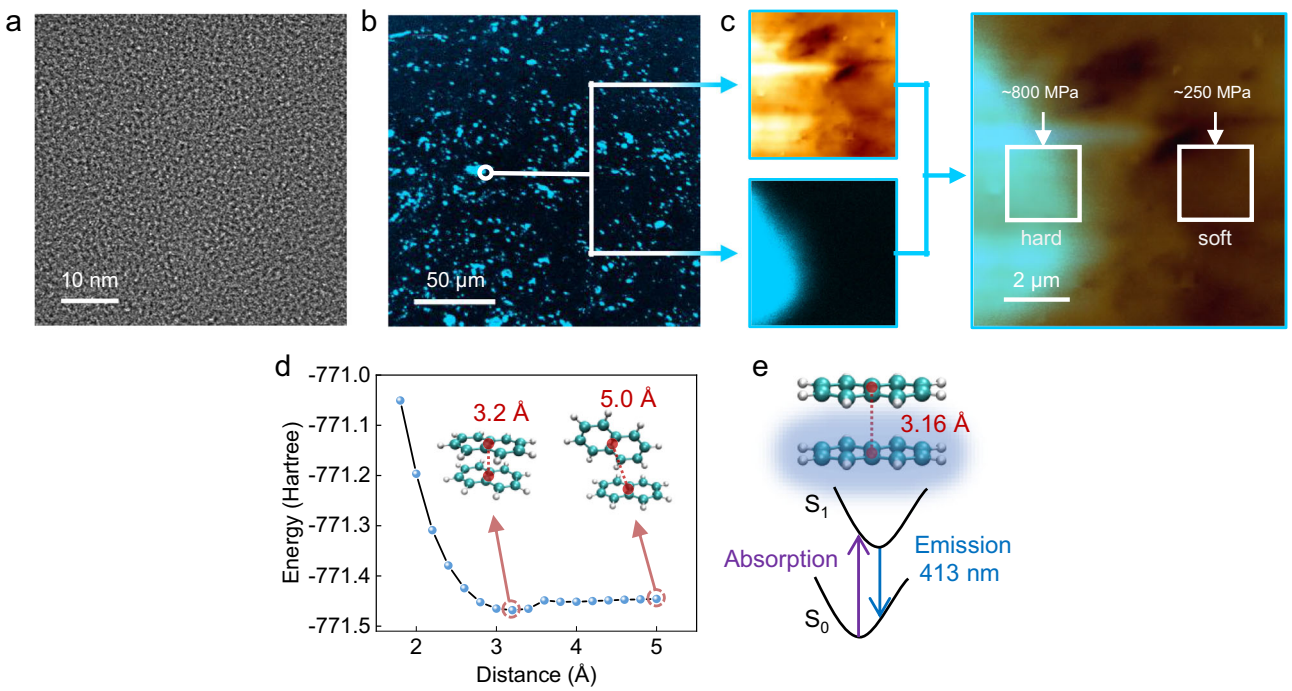

Fig. 6 | Microstructural characterization and theoretical simulation of VN-*co*-IP (PNI). a Transmission electron microscopy (TEM) image of P3 (scale bar: 10 nm). **b** Fluorescence confocal microscopy images of P3. **c** Images of in-situ fluorescence confocal microscopy coupled with atomic force microscopy (AFM) of P3, with modulus mapping: rigid region (left, 800 MPa) and soft region (right, 250 MPa). **d** Potential energy surface (PES) scan of the naphthalene excimer. **e** Unrestricted excited-state optimization at the PES minima and proposed fluorescence mechanism.

To further investigate the polymer-constrained excimer structure, the microstructure of P3 was analyzed by using the transmission electron microscope (TEM) and in situ fluorescence confocal microscopy coupled with atomic force microscopy. As shown in Fig. 6a, b, distinct microphase-separated domains were observed in P3. In the selected area of Fig. 6b, the fluorescent regions exhibited relative modulus three times higher than that of non-fluorescent areas, indicating that the fluorescence of the copolymer arises from the hard phase composed of naphthyl-naphthyl interactions, further confirming the formation of polymer constrained excimers in the harder naphthyl-naphthyl domains under UV (Fig. 6c and Supplementary Fig. 19).

To further explore the fluorescent mechanism in more detail, a potential energy surface (PES) scan of the naphthalene excimer has been conducted, as shown in Fig. 6d. It was revealed that as the center-of-mass distance of the excimer in the excited state decreased from 5 Å, the conformational energy initially reduced and then increased, reaching a minimum at 3.2 Å. A shorter center-of-mass distance corresponded to a higher naphthalene concentration. Additionally, using the geometry with the minimum conformational energy in the excited state, we performed an unrestricted excited-state geometry optimization and calculated the fluorescence emission of the naphthalene excimer, as illustrated in Fig. 6e. The optimized center-of-mass distance was 3.16 Å, closely matching the 3.2 Å from the PES scan. The calculated fluorescence emission wavelength of 413 nm aligned well with the experimental value of 396 nm. These computational findings are consistent with experimental observations and provide a clear explanation for the photoluminescence mechanism of PNI copolymers.

Self-healing fluorescent flexible electrets prepared by PNI copolymer

It was hypothesized that the aggregation of naphthyl groups in a typical aromatic-rich thermoplastic elastomer could impart electret properties, enabling effective charge storage. As shown in Fig. 7a, the corona charging method was used to deposit charges on the surface of the PNI copolymer film with different VN contents by ionizing the air[64]. The surface potential of P6 (201 kDa, 10 mol% VN) decreased rapidly from −1500 V to −12 V in four days, whereas P3 (184 kDa, 27 mol% VN) and P7 (86 kDa, 50 mol% VN) maintained high surface potentials of −766 V and −1039 V, respectively, even after 30 days (Fig. 7b). To clarify the mechanism of charge storage of P3 and P7, the scanning electron microscope (SEM) was used to study their micro morphology. As shown in Supplementary Fig. 20, there were nearly no pores in the polymer film to store charges, revealing that the stability of the deposited charges only relies on the aggregation of naphthyl groups of PNI copolymer. Compared with P6, copolymers P3 and P7 exhibit enhanced charge storage capacity, which may be attributed to their higher T_gs by the higher VN comonomer contents (P6, 10 mol% VN, T_g = −40 °C; P3, 27 mol% VN, T_g = 11 °C; P7, 50 mol% VN, T_g = 70 °C)[65].

Next, a self-healing noncontact single-electrode sensor was fabricated using P3 and a conductive self-healable ionic gel. After the negative polarization of P3 for 30 minutes, it was revealed that P3 exhibited an external electrostatic field due to the deposited charges (Fig. 7c). The surface potential of the metal electrode varied with the distance between the sensor and the metal electrode. The original output voltage was determined to be approximately 6.7 Vpp. After the mechanical damage, the output voltage dramatically decreased to about 3.8 Vpp. When the separated sensor was rejoined and held in contact for a self-healing process for 1 hour, both the PNI copolymer and the conductive ionic gel successfully healed, and the output voltage returned to the original state after healing (Fig. 7d).

A single-electrode sensing system was developed to monitor the motion of a robotic hand. Four sensors were attached to the fingertips of the robotic hand to monitor the bending motion of fingers. As shown in Fig. 7e, a wireless multi-channel measuring circuit was used to measure the output of the sensors and transmit real-time data wirelessly to a cellphone. The movements of robotic fingers can be accurately recorded and displayed through a mobile app by this sensing system. Notably, when exposed to ultraviolet light, the copolymer's fluorescent characteristics enable real-time motion tracking of these robotic fingers - a capability beyond the reach of conventional soft electronics. This feature demonstrates promising applications across

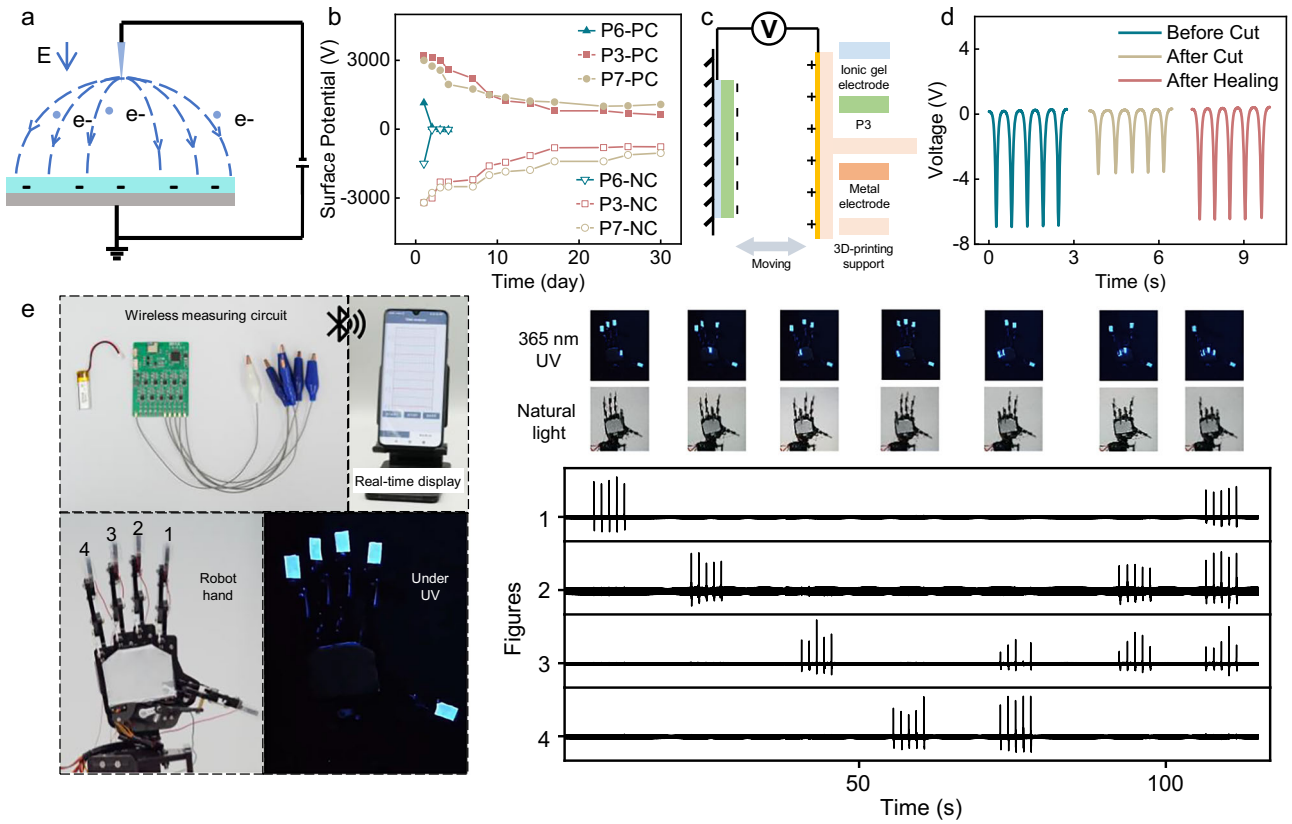

Fig. 7 | Electret properties and device demonstration of VN-*co*-IP (PNI). a Corona polarization setup. **b** Charge retention of the polarized P3, P6, and P7 (PC: positive corona polarization; NC: negative corona polarization). **c** Sensor fabrication. **d** Output voltage: pristine, cut, and healed states. **e** Robotic hand gesture detection under daylight and UV light.

multiple fields such as optically traceable electronic skin, advanced human-machine interfaces (HMI), and deep space exploration systems (Fig. 7e; see also Supplementary Movie 3).

Discussion

In this work, a family of 1-vinylnaphthalene-*co*-isoprene copolymers has been synthesized with different microstructures and sequences. By introducing nanoscale naphthalenyl-naphthalenyl microphase separation into the polyisoprene matrix, these copolymers showed the rare combination of mechanical robustness and intrinsic self-healing capabilities at room temperature without the need for external stimuli. The "polymer-constrained excimers" strategy enables the formation of stable naphthyl-naphthyl excimers under UV stimulation, resulting in an ultra-high photoluminescence quantum yield (PLQY > 98%) in the solid state. Furthermore, the material exhibits superior electret performance with more than 30 days of charge retention. Opto-electromechanical sensors for the robotic hand made from this material can accurately detect finger movements. The autonomously repairable damage, coupled with exceptional optical and electret properties, positions these copolymers as promising candidates for next-generation wearable technologies. Future work will focus on further optimizing the material's performance and exploring its applications in real-world scenarios.

Methods

Materials

Solvents were purified by an MIKROUNA Solv Purer G5 Solvent Purification System and dried over fresh Na chips and molecular sieves in the glovebox (MIKROUNA). 1-Vinylnaphthalene was synthesized according to the literature[66]. Isoprene (IP) and Styrene (St) were purchased from Energy Chemical and purified by distillation from triisobutylaluminium (Al(propyl)$_3$) before use.

1-Naphthaldehyde (97%), Methyltriphenylphosphonium bromide (98%), Potassium tert-butoxide (98%), Isoprene (99%, stabilized with TBC), Styrene (AR, ≥ 99.5%, stabilized with TBC), Methanol (GR, 99.99%; AR, 99.5%), Triisobutylaluminium (1.0 M in *n*-hexane), and sec-Butyllithium (1.3 M *n*-hexane) were obtained from Energy Chemical, Cyclohexane (HPLC, 99.9%) and Tetrahydrofuran (HPLC, 99.9%) were obtained from Yinli. The deuterated solvents Chloroform-d (99.8 atom % D) were obtained from Energy Chemical.

Synthesis of poly(1-vinylnaphthalene-*co*-isoprene) copolymer

General polymerization procedure for the synthesis of poly(1-vinylnaphthalene-*co*-isoprene) copolymers (PNI). Take P3 as an example: In a glovebox, the dried cyclohexane was added into the reaction flask with a magnetic stir bar, followed by the addition of sec-Butyllithium (*s*-BuLi) solution (diluted tenfold before use, 0.10 mL, 0.013 mmol) with 50 mL cyclohexane. The polymerization was started via the addition of the monomer mixture of 1-vinylnaphthalene (1.60 g, 10.4 mmol) and isoprene (1.77 g, 26.0 mmol), and all the reactions were carried out at room temperature under nitrogen. The living chain ends were terminated by the addition of methanol. To precipitate the polymer, the polymer solution was poured into an 8-fold volume excess of methanol, dried at reduced pressure at 60 °C, and a white solid was obtained (2.76 g, yield 81.9%), and stored in the absence of light at room temperature.

Data availability

Additional supporting data are available from the corresponding author upon request.

References

1. Jayathilaka, W. A. D. M. et al. Significance of nanomaterials in wearables: a review on wearable actuators and sensors. *Adv. Mater.* **31**, 1805921 (2019).
2. Yi, F. et al. Wearable energy sources based on 2D materials. *Chem. Soc. Rev.* **47**, 3152–3188 (2018).
3. Lyu, Q., Gong, S., Yin, J., Dyson, J. M. & Cheng, W. Soft wearable healthcare materials and devices. *Adv. Healthc. Mater.* **10**, 2100577 (2021).
4. Wu, Z. et al. Carbon-nanomaterial-based flexible batteries for wearable electronics. *Adv. Mater.* **31**, 1800716 (2019).
5. Park, T., Leem, J. W., Kim, Y. L. & Lee, C. H. Photonic nanomaterials for wearable health solutions. *Adv. Mater.* **n/a**, 2418705.
6. Zhang, Z. Light-emitting materials for wearable electronics. *Nat. Rev. Mater.* **7**, 839–840 (2022).
7. Yang, M. et al. Recent progress in flexible materials for wearable devices for body function and athletic performance monitoring. *Chem. Eng. J.* **505**, 159659 (2025).
8. Rich, S. I., Wood, R. J. & Majidi, C. Untethered soft robotics. *Nat. Electron.* **1**, 102–112 (2018).
9. Gerald, A. & Russo, S. Soft sensing and haptics for medical procedures. *Nat. Rev. Mater.* **9**, 86–88 (2024).
10. Park, J. et al. Soft sensors and actuators for wearable human–machine interfaces. *Chem. Rev.* **124**, 1464–1534 (2024).
11. Wu, Y., Li, Y., Tao, Y., Sun, L. & Yu, C. Recent advances in the material design for intelligent wearable devices. *Mater. Chem. Front.* **7**, 3278–3297 (2023).
12. Zhang, Y., Zheng, X. T., Zhang, X., Pan, J. & Thean, A. V.-Y. Hybrid integration of wearable devices for physiological monitoring. *Chem. Rev.* **124**, 10386–10434 (2024).
13. Yin, S. et al. Wearable and implantable soft robots. *Chem. Rev.* **124**, 11585–11636 (2024).
14. Ding, Y. et al. Porous conductive textiles for wearable electronics. *Chem. Rev.* **124**, 1535–1648 (2024).
15. Won, D. et al. Transparent electronics for wearable electronics application. *Chem. Rev.* **123**, 9982–10078 (2023).
16. Yang, Y. & Gao, W. Wearable and flexible electronics for continuous molecular monitoring. *Chem. Soc. Rev.* **48**, 1465–1491 (2019).
17. Zanchin, G. & Leone, G. Polyolefin thermoplastic elastomers from polymerization catalysis: Advantages, pitfalls and future challenges. *Prog. Polym. Sci.* **113**, 101342 (2021).
18. Langlais, M. et al. Multiblock copolymers based on highly crystalline polyethylene and soft poly(ethylene-co-butadiene) segments: towards polyolefin thermoplastic elastomers. *Angew. Chem. Int. Ed.* **62**, e202310437 (2023).
19. Yang, Y. et al. Terpolymerization of ethylene and two different methoxyaryl-substituted propylenes by scandium catalyst makes tough and fast self-healing elastomers. *Angew. Chem. Int. Ed.* **60**, 26192–26198 (2021).
20. Wang, H. et al. Synthesis of self-healing polymers by scandium-catalyzed copolymerization of ethylene and anisylpropylenes. *J. Am. Chem. Soc.* **141**, 3249–3257 (2019).
21. Wang, S. & Urban, M. W. Self-healing polymers. *Nat. Rev. Mater.* **5**, 562–583 (2020).
22. Chen, Y., Kushner, A. M., Williams, G. A. & Guan, Z. Multiphase design of autonomic self-healing thermoplastic elastomers. *Nat. Chem.* **4**, 467–472 (2012).
23. Zhang, H. et al. Synthesis of self-healing elastomers by scandium-catalyzed terpolymerization of ethylene, styrene, and dimethylaminophenyl-substituted propylene. *Macromolecules* **57**, 7219–7226 (2024).
24. Li, R. et al. Synthesis of self-healing syndiotactic polyolefins by rare-earth catalysts. *ACS Catal.* **14**, 308–317 (2024).
25. Huang, L. et al. Synthesis of tough and fluorescent self-healing elastomers by scandium-catalyzed terpolymerization of pyrenylethenylstyrene, ethylene, and anisylpropylene. *J. Am. Chem. Soc.* **146**, 2718–2727 (2024).

26. Wang, H. et al. Making polyisoprene self-healable through microstructure regulation by rare-earth catalysts. *Angew. Chem. Int. Ed.* **61**, e202210023 (2022).
27. Chung, T. C. Synthesis of functional polyolefin copolymers with graft and block structures. *Prog. Polym. Sci.* **27**, 39–85 (2002).
28. Boaen, N. K. & Hillmyer, M. A. Post-polymerization functionalization of polyolefins. *Chem. Soc. Rev.* **34**, 267–275 (2005).
29. Franssen, N. M. G., Reek, J. N. H. & de Bruin, B. Synthesis of functional 'polyolefins': state of the art and remaining challenges. *Chem. Soc. Rev.* **42**, 5809–5832 (2013).
30. Qu, W., Bi, Z., Zou, C. & Chen, C. Light, heat, and force-responsive polyolefins. *Adv. Sci.* **11**, 2307568 (2024).
31. Zou, C. & Chen, C. Polar-functionalized, crosslinkable, self-healing, and photoresponsive polyolefins. *Angew. Chem. Int. Ed.* **59**, 395–402 (2020).
32. Galikhanov, M. F. Improvement of the electret properties of polystyrene with introduction of titanium dioxide. *Surf. Eng. Appl. Electrochem.* **54**, 111–116 (2018).
33. Talwar, I. M., Srivastava, A. P. & Sinha, H. C. Photo-electret studies of pure and doped polystyrene films. *Polymer* **26**, 1025–1028 (1985).
34. Sonawane, S. L. & Asha, S. K. Fluorescent polystyrene microbeads as invisible security ink and optical vapor sensor for 4-nitrotoluene. *ACS Appl. Mater. Interfaces* **8**, 10590–10599 (2016).
35. Chan, K. M., Kölmel, D. K., Wang, S. & Kool, E. T. Color-change photoswitching of an alkynylpyrene excimer dye. *Angew. Chem. Int. Ed.* **56**, 6497–6501 (2017).
36. Chen, C.-H., Lai, G.-Q. & Luh, T.-Y. Aggregation-enhanced excimer emission of tetraarylethene linkers in ladderphanes. *Macromolecules* **54**, 2134–2142 (2021).
37. Menon, S., Krishnan, A. & Roy, S. Anthracene based photo-tunable polymers with excimer emission. *J. Photochem. Photobiol., A* **406**, 112990 (2021).
38. Fujiki, S., Amaike, K., Yagi, A. & Itami, K. Synthesis, properties, and material hybridization of bare aromatic polymers enabled by dendrimer support. *Nat. Commun.* **13**, 5358 (2022).
39. Gao, Z. et al. A coopetition-driven strategy of parallel/perpendicular aromatic stacking enabling metastable supramolecular polymerization. *Nat. Commun.* **15**, 10762 (2024).
40. Yang, W. et al. Synthetic polymers based on lignin-derived aromatic monomers for high-performance energy-storage materials. *J. Mater. Chem. A* **8**, 24065–24074 (2020).
41. Zheng, S. et al. Monomer design enables mechanistic mapping of anionic ring-opening polymerization of aromatic thionolactones. *Angew. Chem. Int. Ed.* **64**, e202500581 (2025).
42. Rozyyev, V. et al. High-capacity methane storage in flexible alkane-linked porous aromatic network polymers. *Nat. Energy* **4**, 604–611 (2019).
43. Weiss, J. Fluorescence of organic molecules*. *Nature* **152**, 176–178 (1943).
44. Friend, R. H. et al. Electroluminescence in conjugated polymers. *Nature* **397**, 121–128 (1999).
45. Zhu, Y. et al. The balance effect of π–π electronic coupling on NIR-II emission and photodynamic properties of highly hydrophobic conjugated photosensitizers. *Adv. Sci.* **11**, 2307569 (2024).
46. Qi, J., Ou, H., Liu, Q. & Ding, D. Gathering brings strength: How organic aggregates boost disease phototheranostics. *Aggregate* **2**, 95–113 (2021).
47. Uchida, K., Tanaka, M. & Tomura, M. Excimer emission of crystalline naphthalene. *J. Lumin.* **20**, 409–414 (1979).
48. Ghiggino, K. P., Wright, R. D. & Phillips, D. Excimer dissociation in poly(1-vinyl naphthalene). *Chem. Phys. Lett.* **53**, 552–554 (1978).
49. Azumi, T. & Azumi, H. The lifetime of excimer fluorescence of naphthalene. *Bull. Chem. Soc. Jpn.* **39**, 2317–2320 (2006).
50. Parolin, G. et al. Conformational dynamics of the pyrene excimer. *PCCP* **26**, 29351–29363 (2024).
51. Chawdhury, D. R., Narayanan, S., Agrawal, T. & Bisht, P. B. Excimer formation and site selectivity in single pyrene microcrystals. *J. Lumin.* **263**, 120084 (2023).
52. Vollbrecht, J. Excimers in organic electronics. *N. J. Chem.* **42**, 11249–11254 (2018).
53. Hartmann Schatloff, D., Retamal Altbir, C. & Valenzuela, F. The role of excimer light in dermatology: a review. *Bras. Dermatol.* **99**, 887–894 (2024).
54. Matejdes, M. et al. Excimer formation in a 2D confined space. *Mater. Today Chem.* **42**, 102436 (2024).
55. Kim, T.-I., Jin, H., Bae, J. & Kim, Y. Excimer emission-based fluorescent probe targeting caspase-3. *Anal. Chem.* **89**, 10565–10569 (2017).
56. Zhang, Z. & Ren, S. Metal-cluster-based colloidal excimer superstructures. *Angew. Chem. Int. Ed.* **55**, 15708–15710 (2016).
57. Li, X. et al. Polymer electrets and their applications. *J. Appl. Polym. Sci.* **138**, 50406 (2021).
58. Chortos, A., Liu, J. & Bao, Z. Pursuing prosthetic electronic skin. *Nat. Mater.* **15**, 937–950 (2016).
59. Huynh, W. U. et al. Hybrid nanorod-polymer solar cells. *Science* **295**, 2425–2427 (2002).
60. Wang, Z. & Song, J. Piezoelectric nanogenerators based on zinc oxide nanowire arrays. *Science* **312**, 242–246 (2006).
61. Venkatasubramanian, R. et al. Thin-film thermoelectric devices with high room-temperature figures of merit. *Nature* **413**, 597–602 (2001).
62. Jung, S., Lee, J., Hyeon, T., Lee, M. & Kim, D. H. Fabric-based integrated energy devices for wearable activity monitors. *Adv. Mater.* **26**, 6329 (2014).
63. Steube, M. et al. Isoprene/styrene tapered multiblock copolymers with up to ten blocks: synthesis, phase behavior, order, and mechanical properties. *Macromolecules* **51**, 10246–10258 (2018).
64. Du, G. et al. Compliant iontronic triboelectric gels with phase-locked structure enabled by competitive hydrogen bonding. *Nano-Micro Lett.* **16**, 170 (2024).
65. Mishra, A. Studies of polymer electrets. II. Factors governing the stabilities of homoelectrets obtained from polystyrene and its derivatives. *J. Appl. Polym. Sci.* **27**, 1107–1118 (1982).
66. Khan, Z. A., Iwaoka, M. & Wirth, T. Novel cyclization cascades to functionalized indanes and tetrahydronaphthalenes. *Tetrahedron* **66**, 6639–6646 (2010).
67. Fries, F. & Reineke, S. Statistical treatment of photoluminescence quantum yield measurements. *Sci. Rep.* **9**, 15638 (2019).
68. de Mello, J. C., Wittmann, H. F. & Friend, R. H. An improved experimental determination of external photoluminescence quantum efficiency. *Adv. Mater.* **9**, 230–232 (1997).
69. Song, B. et al. Facile conversion of water to functional molecules and cross-linked polymeric films with efficient clusteroluminescence. *Nat. Commun.* **14**, 3115 (2023).
70. Li, C. et al. Self-assembled small molecule spherulites under mild conditions: High solid-state quantum yield and unique interconnected structural and fluorescent colors. *Aggregate* **6**, e695 (2025).
71. Baysec, S., Preis, E., Allard, S. & Scherf, U. Very high solid state photoluminescence quantum yields of poly(tetraphenylethylene) derivatives. *Macromol. Rapid Commun.* **37**, 1802–1806 (2016).
72. Leventis, A. et al. Highly luminescent encapsulated narrow band-gap polymers based on diketopyrrolopyrrole. *J. Am. Chem. Soc.* **140**, 1622–1626 (2018).
73. Christopherson, C. J. et al. 1,8-naphthalimide-based polymers exhibiting deep-red thermally activated delayed fluorescence and their application in ratiometric temperature sensing. *ACS Appl. Mater. Interfaces* **12**, 20000–20011 (2020).

74. Aniés, F. et al. A conjugated carboranyl main chain polymer with aggregation-induced emission in the near-infrared. *J. Am. Chem. Soc.* **146**, 13607–13616 (2024).
75. Shao, S. et al. Blue thermally activated delayed fluorescence polymers with nonconjugated backbone and through-space charge transfer effect. *J. Am. Chem. Soc.* **139**, 17739–17742 (2017).

Acknowledgements

This work was supported, in part, by the National Key R&D Program of China (No.2022YFE0103800), the National Natural Science Foundation of China (No.22171091), the Guangdong Basic and Applied Basic Research Foundation (No. 2022A1515011785, 2024 A1515011330), the Introduced Innovative R&D Team of Guangdong (2021ZT09L392), the Pearl River Talent Recruitment Program (2021QN020782), the Science and Technology Program of Guangzhou (2024D03J0003). This work is partially supported by High Performance Computing Platform of South China University of Technology. We are grateful to Professor Zhiguo Xia, Wei Liao, and Zhan Xiong for the measurement of quantum yield. The university logo in Fig. 4A has obtained the usage permission.

Author contributions

H.W. and S.Z. conceived and designed the experiments. S.Z. performed the synthesis, mechanical, self-healing, and optical experiments, and analyzed the data. D.Z. and J. Z. conceived and designed the electrets application. N.C. and J.Z. conceived computational studies. S.Z., D.Z., N.C., and H.W. prepared the manuscript. S.Z., D.Z., and N.C contributed equally. H.W. directed the project.

Competing interests

The authors declare no competing interests.

Additional information

Supplementary information The online version contains supplementary material available at https://doi.org/10.1038/s41467-025-65539-9.

Correspondence and requests for materials should be addressed to Jiajia Zhou, Junwen Zhong or Haobing Wang.

Peer review information *Nature Communications* thanks Kenjiro Fukuda and the other anonymous reviewer(s) for their contribution to the peer review of this work. A peer review file is available.

Supplementary Information

Polymer-Constrained Excimer Enables Flexible and Self-Healable Optoelectronic Materials for Wearable Sensor

Shuyu Zheng,[1,2] Dazhe Zhao,[3] Nengjie Cao,[1] Jiajia Zhou,[1,2,*] Junwen Zhong, [3,*] Haobing Wang [1,2,*]

Author affiliations:

1 Advanced Institute for Soft Matter Science and Technology (AISMST), School of Emergent Soft Matter, South China University of Technology 510640 Guangzhou, China

2 Guangdong Provincial Key Laboratory of Functional and Intelligent Hybrid Materials and Devices, Guangdong Basic Research Center of Excellence for Energy and Information Polymer Materials, South China University of Technology, 510640 Guangzhou, China

3 Department of Electromechanical Engineering and Centre for Artificial Intelligence and Robotics, University of Macau, Macau, SAR 999078, China

*Correspondence to: junwenzhong@um.edu.mo (J. Zhong), zhouj2@scut.edu.cn (J. Zhou), haobingwang@scut.edu.cn (H. Wang)

Supplementary Table of the content

70 mol%), and **b**) PNI copolymer (27-28 mol% VN) with different molecular weight (117, 143, 184, 201, and 227 kDa).

Supplementary Fig. 5. ^{1}H DOSY NMR spectrum of P1. ^{1}H DOSY NMR spectrum (400 MHz, $CDCl_3$) with 1D spectrum shown at the top of P1.

Supplementary Fig. 6. NMR test of copolymer. ^{13}C-NMR spectrum (100 MHz, $CDCl_3$) of P3.

Supplementary Fig. 7. Thermogravimetric Analysis (TGA) of PNI copolymers. Thermo Gravimetric Analysis (TGA) of PNI copolymer with different contents of VN: 10, 20, 25, 30, 35, 40, 50, and 70 mol%.

Supplementary Table 2. Mechanical test of copolymer. Stress-strain test of PNI copolymers.

Supplementary Fig. 8. Mechanical test of copolymer. Cyclic stress-strain test for P3.

Supplementary Fig. 9. Self-healing test of P5 and PNI with 35 mol% VN. **a**) Self-healing test of P5. **b**) Self-healing test of PNI copolymer (180 kDa, 35 mol% VN). **c**) Self-healing comparison of P3 self-healed under room temperature and human body temperature, and P5 self-healed under room temperature.

Supplementary Fig. 10. Dynamic mechanical analysis of PNI copolymer. Dynamic mechanical analysis of **a**) PNI copolymer with different contents of VN (10, 30, and 50 mol%), and **b**) PNI copolymer of 27 mol% VN with different molecular weight (117, 184, and 227 kDa).

Supplementary Fig. 11. Dynamic mechanical analysis of PNI copolymer and segmented copolymer. Dynamic mechanical analysis of PNI copolymer with 184 kDa and 27 mol% VN (top) and segmented copolymer of NIN-3 (bottom, 22 kDa, 30 mol% VN).

Supplementary Fig. 12. Rheological measurement curves of PNI copolymer. Rheological measurement curves: Storage modulus of PNI copolymer (M_n = 24 ± 4 kDa) with **a**) 10 mol% VN, **b**) 30 mol% VN, and **c**) 50 mol% VN. Loss modulus of PNI copolymer with **d**) 10 mol% VN, **e**) 30 mol% VN, and **f**) 50 mol% VN.

Supplementary Fig. 13. Rheological measurement curves of PNI copolymer. Rheological measurement curves: Storage modulus of PNI copolymer (27 mol% VN) with M_n = **a**) 117 kDa, **b**) 184 kDa, and **c**) 227 kDa. Loss modulus of PNI copolymer (27 mol% VN) with M_n = **d**) 117 kDa, **e**) 184 kDa, and **f**) 227 kDa.

Supplementary Fig. 14. Rheological measurement curves of PNI copolymer and segmented copolymer. Rheological measurement curves: Storage modulus of **a**) P3, **b**) segmented copolymer of NIN-3. Loss modulus of **c**) P3, **d**) NIN-3.

Supplementary Fig. 15. Schematic diagram of the test principle. Measurement of quantum yield of P3 film using the integrating sphere.

Supplementary Fig. 16. Fluorescence test of copolymer. The fluorescence intensity variation of P3 during self-healing process.

Supplementary Fig. 17. Fluorescent spectra of Naphthalene and PNI copolymer dissolved in THF. **a**) Naphthalene dissolved in THF (1 mM). **b**) P3 dispersed in THF (18 g/L).

Supplementary Fig. 18. Fluorescence test of copolymer. Fluorescent emission spectra of PNI copolymer with different content of VN (10, 20, 25, 30, 35, 40, and 50 mol%).

Supplementary Fig. 19. Fluorescent confocal test of copolymer. The 3D reconstruction of P3 block by Z-stack scan of the fluorescent confocal microscope.

Supplementary Fig. 20. Scanning electron microscope (SEM) images and BET test result of P3. **a**) and **b**) Scanning electron microscope (SEM) images of P3. **c**) Pore size distribution curve of P3 gained by Brunauer-Emmett-Teller test (BET Surface Area: 0.4417 m^2/g).

1. Supplementary Methods

Characterizations. Nuclear magnetic resonance (NMR) spectra were recorded on a 400/100 MHz (Bruker, Fällanden, Switzerland) (FT, 400 MHz for ^{1}H; 100 MHz for ^{13}C) spectrometer with $CDCl_3$ as solvent. Chemical shifts were referenced to the signal of the solvent (residual proton resonances for ^{1}H spectra, carbon resonances for ^{13}C spectra).

Molecular weights and molecular-weight distributions of the polymers were determined by gel permeation chromatography (GPC). Thermal gravimetric analysis (TGA) on a Mettler Toledo TGA/DSC 3+ STARe System, TA Instrument, was used to determine the decomposition temperature of polymers; the samples were heated from ambient temperature to 900 ℃ at a rate of 10 ℃ min^{-1}.

Differential scanning calorimetry (DSC) measurements were performed on a DSC (Mettler Toledo DSC 3). Polymer samples were weighed (typically in a 3-5 mg range) and sealed in hermetic aluminum pans using a DSC press. The samples were first heated to 250 ℃ at 10 ℃ min^{-1}, equilibrated at this temperature for 5 min, then cooled to −60 ℃ at 10 ℃ min^{-1}, held at this temperature for 5 min, and reheated to 250 ℃ at 10 ℃ min^{-1} under a nitrogen flow (50 mL/min). All T_g values were obtained from the second scan.

The viscoelastic properties of polymers were analyzed using a Discovery DMA 850. The testing was made in compression mode at 200

mN with heating from −75 to 240 °C at a heating rate of 10 °C min^{-1} and a fixed frequency of 1 Hz. Rheological measurements were carried out by Anton Paar 302e, Austria. The samples were tested from −30 to 150 °C, with an angular frequency from 0.1 to 100 rad/s.

Mechanical tensile-stress experiments were performed using an Instron 68SC-1 instrument. Three samples were tested for each polymer composition. Tensile experiments were performed at room temperature (25 ± 1 °C) at different sample size and strain rate when evaluating the stretchability according to ASTM 882-09 test method using dumbbell-conFig.d specimens according to JIS K-6251-7 (width: 2 mm; length: 12 mm; thickness: 1 mm). Strain at break and stress at break experiment was determined at fracture using uniaxial tensile test with a strain rate of 300 mm/min. Young's modulus is the initial slope of the nominal stress vs nominal strain curve in the linear region ($0 < \varepsilon < 0.05$) and was calculated from the average of three monotonic curves. Cyclic stress-strain test for P3 was carried out with a strain rate of 300 mm/min and release rate of 300 mm/min. Strain recovery was determined by a 550 % strain step cycle test using the equation $100\ (\varepsilon_a - \varepsilon_r)/\varepsilon_a$, where ε_a = applied strain and ε_r = strain at zero load after 10th cycle.

For self-healing tests, the sample was cut into separate parts completely using razor blade. The break surface of films was contacted in air. The cut faces were brought together and gently pressed for less than 15

seconds at 25 °C. The healed polymer films were then stretched following the same procedure to obtain the stress-strain curves. The mechanical healing efficiency was defined as the ratio between the fracture strain restored relative to the original fracture strain.

Transmission Electron Microscopy (TEM) images were taken by Talos F200X. Visible light transmittance spectrum was taken by SHIMADZU UV-3600 PLUS, the sample is made by hot-pressing with a thickness of 50 μm.

Fluorescent (FL) excitation and emission spectra were taken by HITACHI F-4700. The liquid samples were tested by using quartz cell, and the solid samples were tested by being fixed on a professional fixture. The quantum yields of the samples were taken by Quantaurus-QY Plus C13534-11, Hamamatsu Photonics, and calculated by the bundled software. Fluorescent optical images were taken by one of two confocal laser scanning microscopy (CLSM) systems, Leica TCS SP8 STED or Zeiss SLM 880. Scanning electron microscope (SEM) images were taken by SIGA 300.

Brunauer-Emmett-Teller test was taken by Micromeritics ASAP 2460. The sample is made by hot-pressing and cut into small pieces, then the sample was put into the glass container and dried at reduced pressure under 80 °C by Micromeritics VacPrep 061 Sample Degas System over night and used for the following test.

The corona charging of the PNI copolymer film was taken by Dongwen DW-P303-1ACD1 (High Voltage Power Supply). The surface potential of the samples is measured by an electrostatic voltmeter (Trek 347). The output current and voltage of the samples are measured by a Keithely 6514 electrometer and an NI USB 6341 data acquisition system.

The calculation of reactivity ratio. The reactivity ratios of IP and VN were calculated by linear fitting, and the raw data were taken from ^{1}H NMR spectra of PNI copolymerization with different feed ratio. The reactivity ratio of IP and VN can be expressed by equations as follows:

$$\frac{d[M_1]}{d[M_2]} = \frac{[M_1]}{[M_2]} \cdot \frac{r_1[M_1]+[M_2]}{r_2[M_2]+[M_1]} \quad (1)$$

where $d[M_1]$ and $d[M_2]$ are respectively the substance amount of M_1 and M_2 in the copolymer chain at a certain moment, $[M_1]$ and $[M_2]$ are respectively the substance amount of monomer M_1 and M_2, r_1 and r_2 are respectively the reactivity ratio of monomer M_1 and M_2.

$$R = \frac{[M_1]}{[M_2]} \quad (2)$$

where R is the initial molar ratio of the two monomers.

$$\rho = \frac{d[M_1]}{d[M_2]} \quad (3)$$

where ρ is the molar ratio of the two monomer units in the copolymer produced at this instant.

According to equation (1), (2), and (3), the equation (1) can be expressed as follows:

$$\frac{R(\rho-1)}{\rho} = \frac{R^2}{\rho} r_1 - r_2 \quad (4)$$

The calculated result is shown in Supplementary Fig. 2c.

The calculation of photoluminescence quantum yield. The IUPAC definition of (integral) quantum yield, $\Phi(\lambda)$ is [1]:

$$\Phi\ (\lambda) = \frac{\text{number of events}}{\text{number of photons absorbed}} \tag{5}$$

where $\Phi\ (\lambda)$ can be used for photophysical processes. More usually, it is written for emission of light:

$$\Phi\ (\lambda) = \frac{\text{number of photons emitted}}{\text{number of photons absorbed}} \tag{6}$$

To determine the PLQY Φ, we use the de Mello method with three measurements, as shown in Supplementary Fig. 15. First, the excitation is led into the empty sphere to quantify the excitation intensity (empty sphere, coded as A). Second, the sample is placed within the sphere, but not in the excitation beam (indirect illumination of the sample, coded as B). Third, the sample has to be placed directly in the excitation beam (direct illumination, coded as C). For a wavelength scale, the integration in each case should be with respect to $\int \frac{\lambda}{hc} d\lambda$, and each spectrum taken consists of two parts: the residual excitation light and the emitted light. Both parts are integrated separately and are referred to as X (excitation) and E (emission), with a subscript denoting the respective measurement. With this, the absorption A and finally the PLQY Φ can be calculated [2, 3, 4]:

$$A = (1 - \frac{X_\mathrm{C}}{X_\mathrm{B}}) \tag{7}$$

$$\Phi = \frac{E_\mathrm{C} - (1-A)E_\mathrm{B}}{A \cdot X_\mathrm{A}} \tag{8}$$

2. Supplementary Figures and Tables

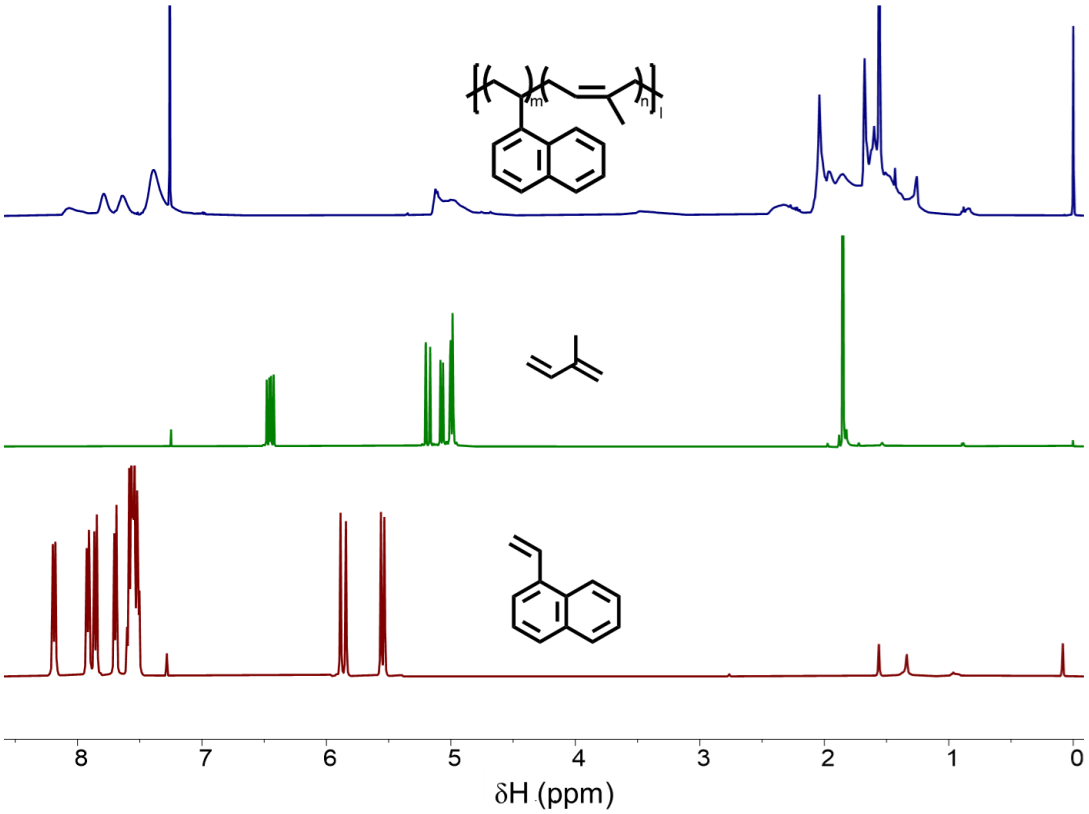

Supplementary Fig. 1. Reaction processes characterization of PNI copolymer. ^{1}H-NMR spectrum (400 MHz, $CDCl_3$) of poly(1-vinylnaphthalene-*co*-isoprene) copolymer (PNI), isoprene (IP), and 1-vinylnaphthalene (VN).

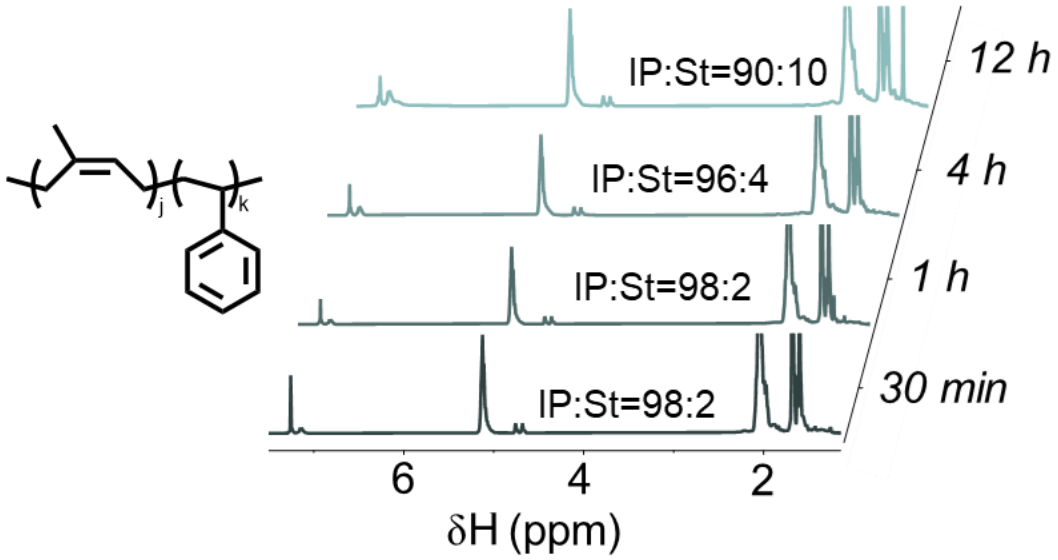

Supplementary Fig. 2. Reaction processes characterization of IP and styrene copolymer. ^{1}H NMR spectra of tracing the copolymerization of IP with styrene (St), (400 MHz, $CDCl_3$).

Supplementary Table 1. Preparation of copolymer. Copolymerization of isoprene (IP) and 1-vinylnaphthalene (VN).

Polymer type	[**IP**] : [**VN**] : [*s*-BuLi][b]	conv. **IP** (%)	conv. **VN** (%)	M_n ($\times 10^3$ g mol^{-1})[c]	**IP**/**VN**[d]	M_w/M_n[c]	T_g (°C)[e]
Random	310 : 40 : 1	95 %	81 %	28	90/10	1.1	−45
Random	280 : 70 : 1	90 %	85 %	27	80/20	1.2	−30
Random	240 : 110 : 1	95 %	89 %	25	70/30	1.2	5
Random	190 : 160 : 1	94 %	75 %	23	60/40	1.1	40
Random	160 : 190 : 1	84 %	70 %	21	50/50	1.1	70
Random	80 : 270 : 1	79 %	54 %	19	30/70	1.1	100
Homo	0 : 350 : 1	/	59 %	10	0/100	2.7	120
Random	1550 : 550 : 1	91 %	85 %	123	75/25	1.1	9
Random	1500 : 600 : 1	96 %	82 %	117	73/27	1.1	10
Random	1800 : 720 : 1	95 %	82 %	143	72/28	1.6	10
Random	2000 : 800 : 1	92 %	79 %	184	73/27	2.5	11
Random	2200 : 880 : 1	90 %	78 %	201	73/27	2.3	13
Random	2500 : 1000 : 1	90 %	77 %	227	73/27	2.3	15
Random	2500 : 300 : 1	90 %	83 %	201	90/10	1.5	−40
Random	1700 : 1100 : 1	89 %	74 %	180	65/35	3.5	20
Random	800 : 950 : 1	77 %	65 %	86	50/50	3.6	70
Segmented	240 : 110 : 1	83 %	78 %	22	70/30	1.5	90

a) Conditions: Sec-Butyllithium (*s*-BuLi) (1.3×10^{-2} mmol); 50 mL Cyclohexane; Room temperature. **b**) Feed ratio (in moles) of isoprene (IP), 1-vinylnaphthalene (VN), and *s*-BuLi. **c**) Determined by gel permeation chromatography (GPC) in tetrahydrofuran (THF) at 35 °C against polystyrene standard (Supplementary Fig. 4). M_n = number-average molecular weight, M_w = weight-average molecular weight. **d**) Molar ratio of IP and VN in the copolymer, determined by ^{1}H nuclear magnetic resonance (NMR) analysis. **e**) Determined by differential scanning calorimetry (DSC).

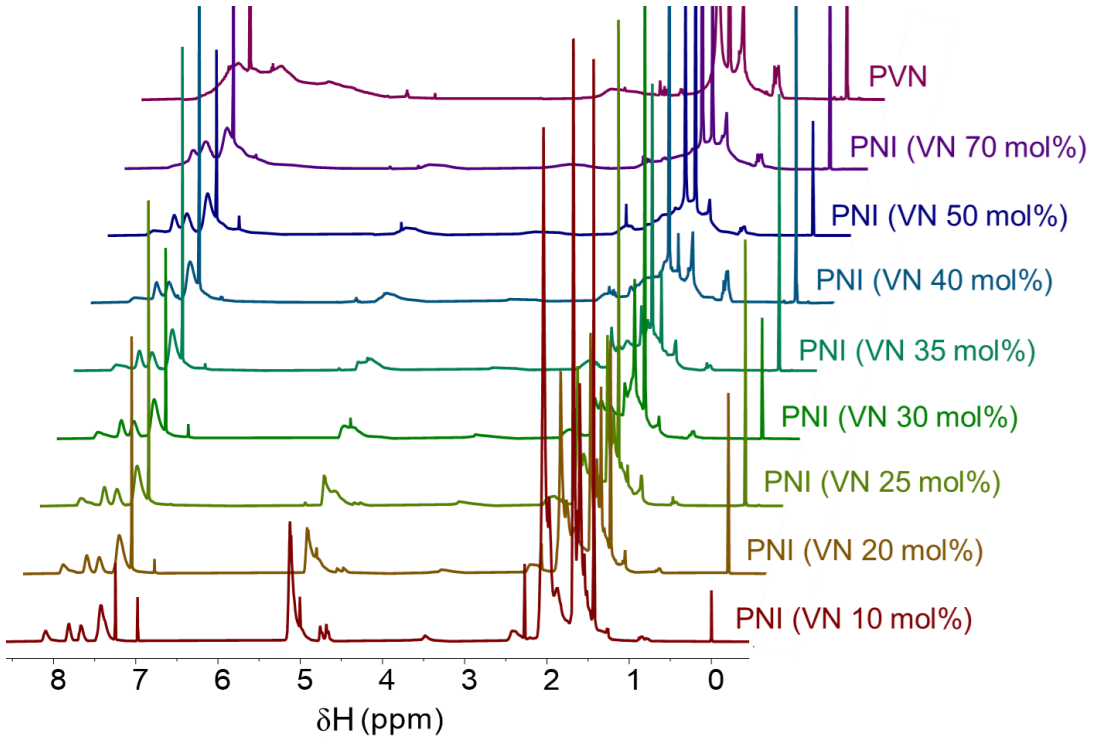

Supplementary Fig. 3. ^{1}H-NMR spectrum of PNI copolymer and PVN. ^{1}H-NMR spectrum (400 MHz, $CDCl_3$) of poly(1-vinylnaphthalene) (PVN) and poly(1-vinylnaphthalene-*co*-isoprene) copolymer (PNI) with different contents of 1-vinylnaphthalene (VN): 10, 20, 25, 30, 35, 40, 50, and 70 mol%.

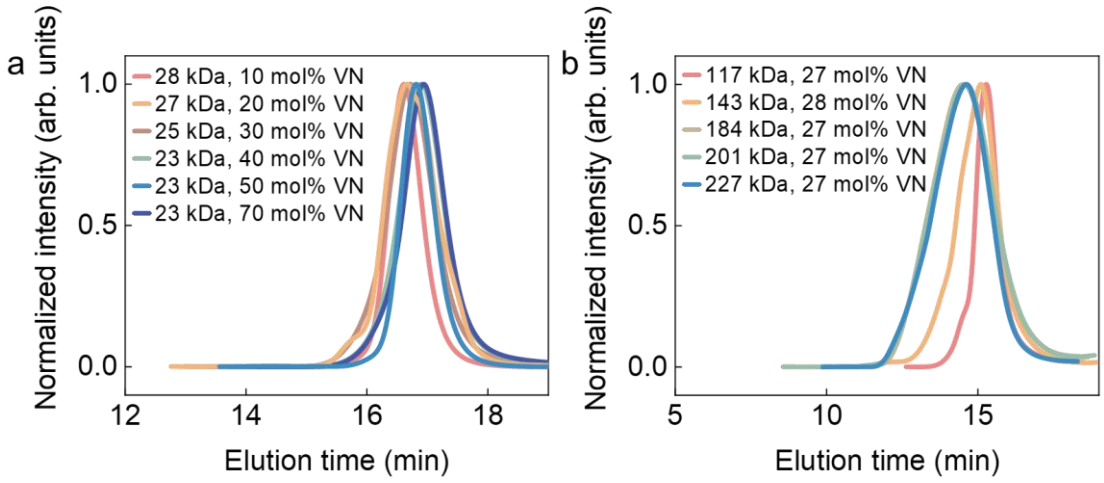

Supplementary Fig. 4. GPC curve of PNI copolymer. **a**) PNI copolymer (25 ± 5 kDa) with different content of VN (10, 20, 30, 40, 50, and 70 mol%), and **b**) PNI

copolymer (27-28 mol% VN) with different molecular weight (117, 143, 184, 201, and 227 kDa).

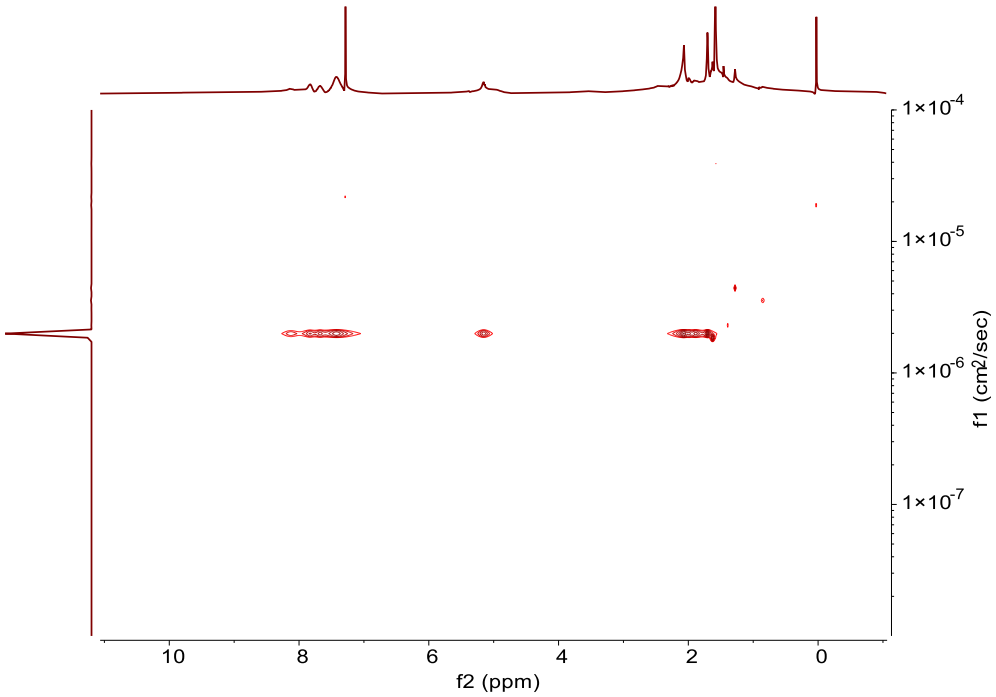

Supplementary Fig. 5. ^{1}H DOSY NMR spectrum of P1. ^{1}H DOSY NMR spectrum (400 MHz, $CDCl_3$) with 1D spectrum shown at the top of P1.

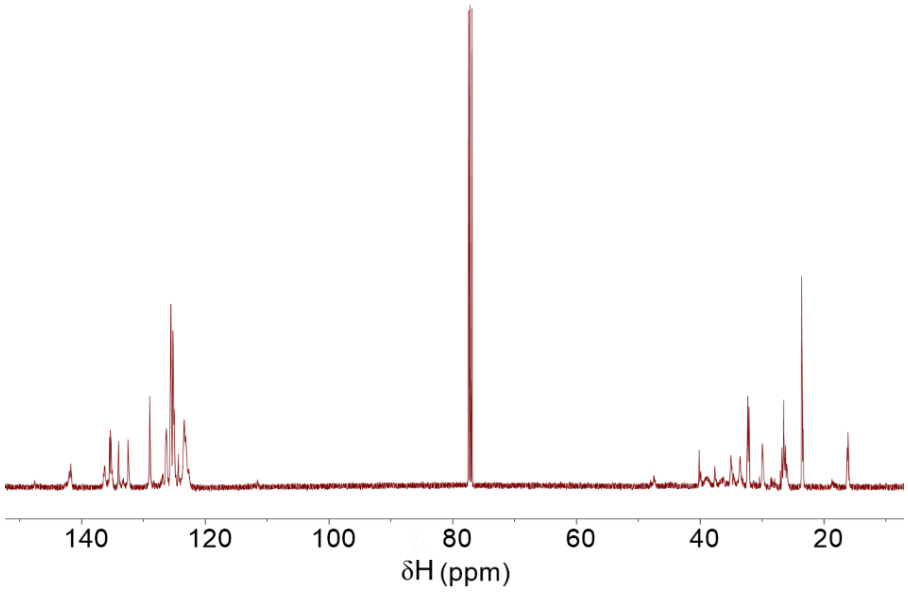

Supplementary Fig. 6. NMR test of copolymer. Typical ^{13}C-NMR spectrum (100 MHz, $CDCl_3$) of copolymer (P3).

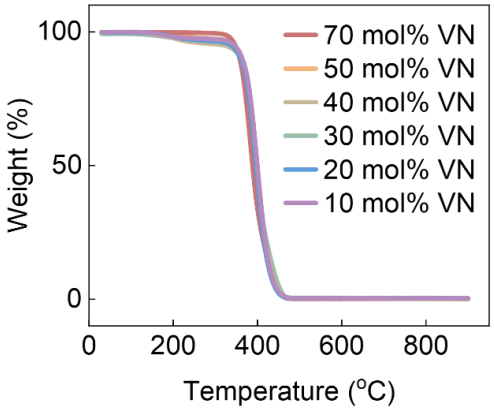

Supplementary Fig. 7. Thermogravimetric Analysis (TGA) of PNI copolymers. Thermogravimetric Analysis (TGA) of PNI copolymers with different VN content: 10, 20, 25, 30, 35, 40, 50, and 70 mol%.

Supplementary Table 2. Mechanical test of copolymer. Stress-strain test of PNI copolymers.

Content of VN (mol%) [a]	M_n ($\times 10^3$ g mol^{-1}) [b]	breaking strength (MPa) [c]	elongation at break (%) [c]	Young's modulus (MPa) [c]	Toughness (MJ m^{-3}) [c]
10	28	0.14 ± 0.01	1460 ± 20	0.1 ± 0.05	2.3 ± 0.1
30	25	1 ± 0.1	2020 ± 20	0.5 ± 0.1	15 ± 1
40	23	25 ± 1	300 ± 10	100 ± 2	89 ± 2
50	21	24 ± 1	5 ± 1	460 ± 5	1.45 ± 0.05
70	19	13 ± 1	2 ± 1	400 ± 10	0.50 ± 0.05
27	117	2.4 ± 0.1	1950 ± 10	0.7 ± 0.1	31 ± 1
28	143	3 ± 0.5	1890 ± 5	5 ± 0.5	40 ± 1
27	184	12 ± 0.5	1450 ± 5	8 ± 1	95 ± 2
27	201	20 ± 1	1300 ± 5	13 ± 0.5	170 ± 3
27	227	25 ± 1	1200 ± 20	14 ± 1	180 ± 2

a) Molar ratio of 1-vinylnaphthalene (VN) in the copolymer, determined by ^{1}H nuclear magnetic resonance (NMR) analysis. b) Determined by gel permeation chromatography (GPC) in tetrahydrofuran (THF) at 35 °C against polystyrene standard (Supplementary

Fig. 4). M_n = number-average molecular weight. c) Determined by Stress-strain curves of PNI copolymer.

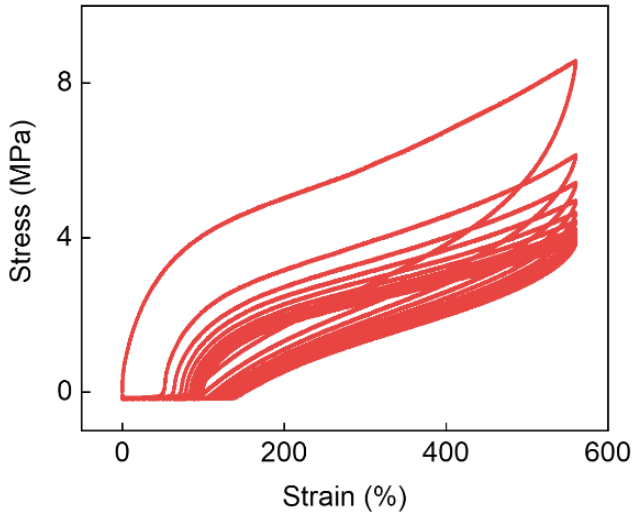

Supplementary Fig. 8. Mechanical test of copolymer. Cyclic stress-strain test for P3.

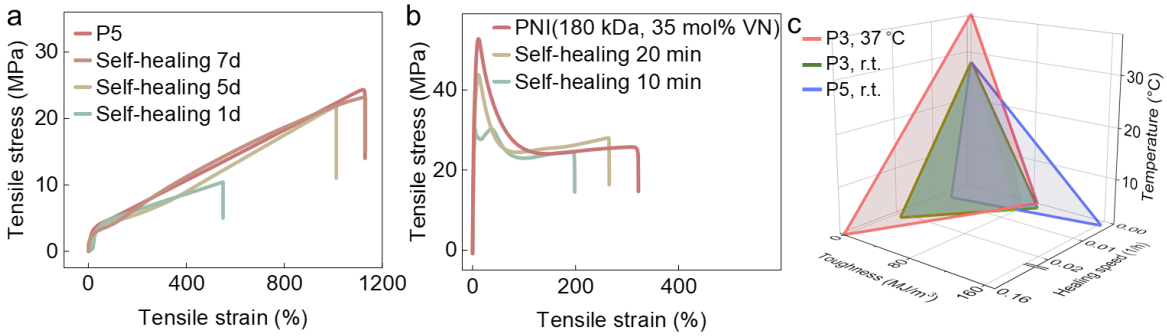

Supplementary Fig. 9. Self-healing test of P5 and PNI with 35 mol% VN. **a**) Self-healing test of P5. **b**) Self-healing test of PNI copolymer (180 kDa, 35 mol% VN). **c**) Self-healing comparison of P3 self-healed under room temperature and human body temperature, and P5 self-healed under room temperature.

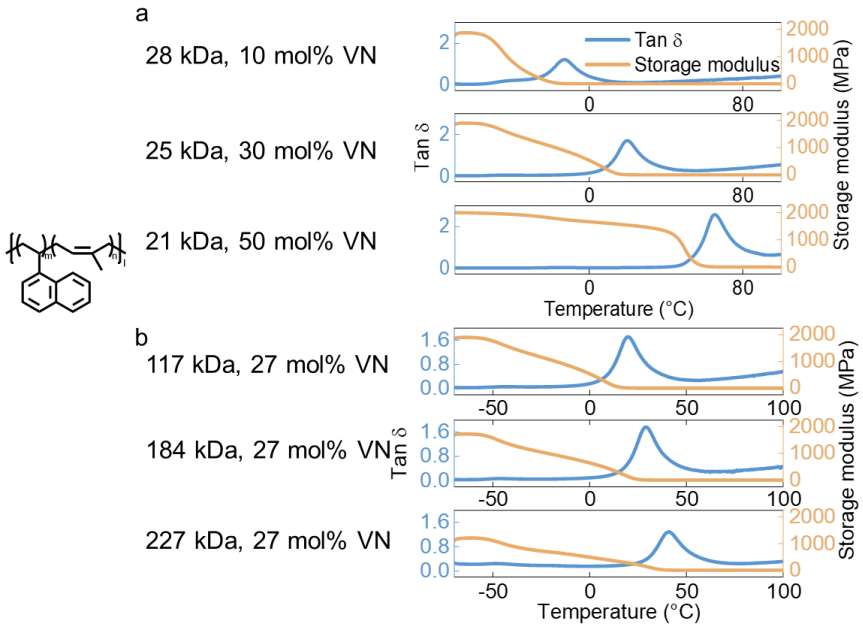

Supplementary Fig. 10. Dynamic mechanical analysis of PNI copolymer. Dynamic mechanical analysis of **a**) PNI copolymer with different contents of VN (10, 30, and 50 mol%), and **b**) PNI copolymer of 27 mol% VN with different molecular weight (117, 184, and 227 kDa).

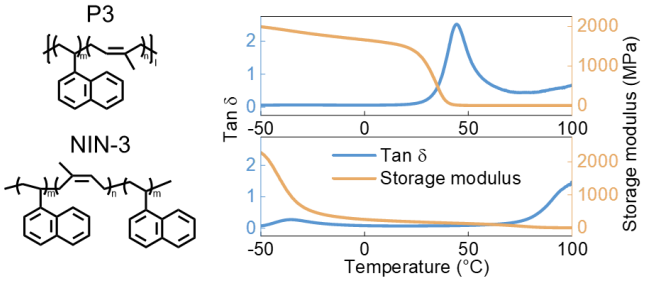

Supplementary Fig. 11. Dynamic mechanical analysis of PNI copolymer and segmented copolymer. Dynamic mechanical analysis of PNI copolymer with 184 kDa and 27 mol% VN (top) and segmented copolymer of NIN-3 (bottom, 22 kDa, 30 mol% VN).

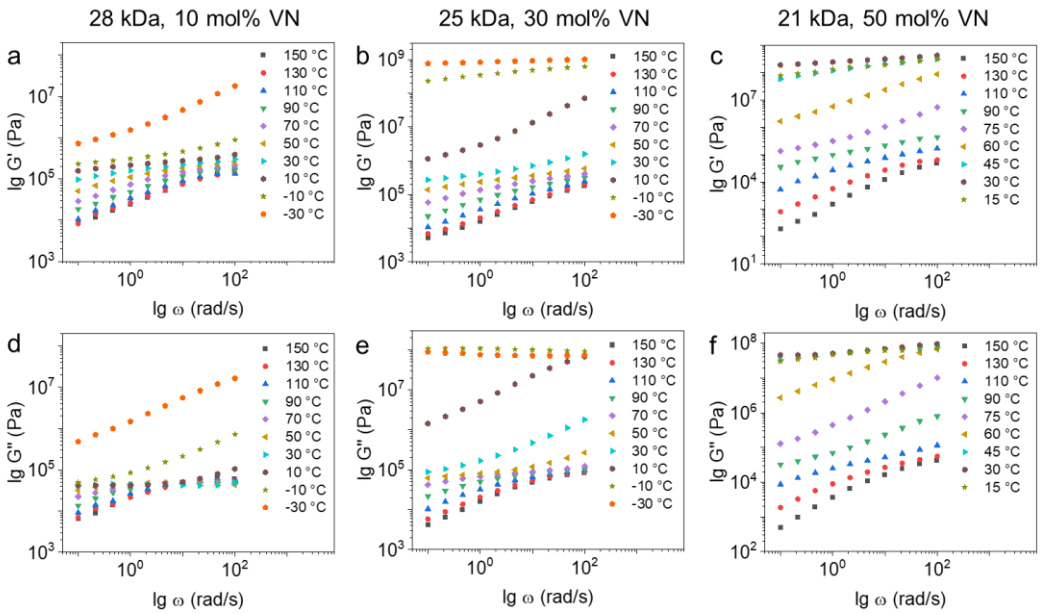

Supplementary Fig. 12. Rheological measurement curves of PNI copolymer. Rheological measurement curves: Storage modulus of PNI copolymer (M_n = 24 ± 4 kDa) with **a**) 10 mol% VN, **b**) 30 mol% VN, and **c**) 50 mol% VN. Loss modulus of PNI copolymer with **d**) 10 mol% VN, **e**) 30 mol% VN, and **f**) 50 mol% VN.

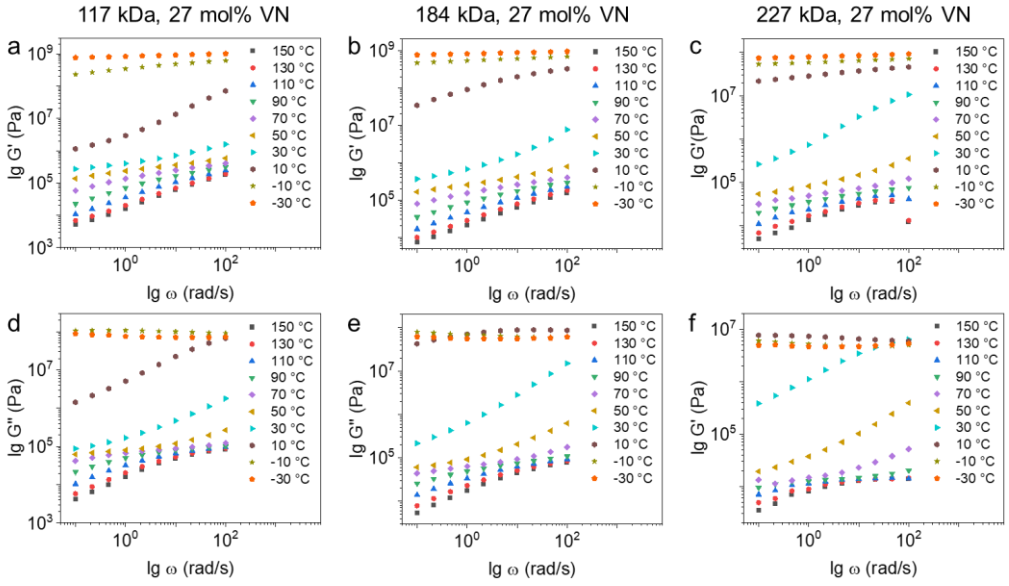

Supplementary Fig. 13. Rheological measurement curves of PNI copolymer. Rheological measurement curves: Storage modulus of PNI copolymer (27 mol% VN) with M_n = **a**) 117 kDa, **b**) 184 kDa, and **c**) 227 kDa. Loss modulus of PNI copolymer (27 mol% VN) with M_n = **d**) 117 kDa, **e**) 184 kDa, and **f**) 227 kDa.

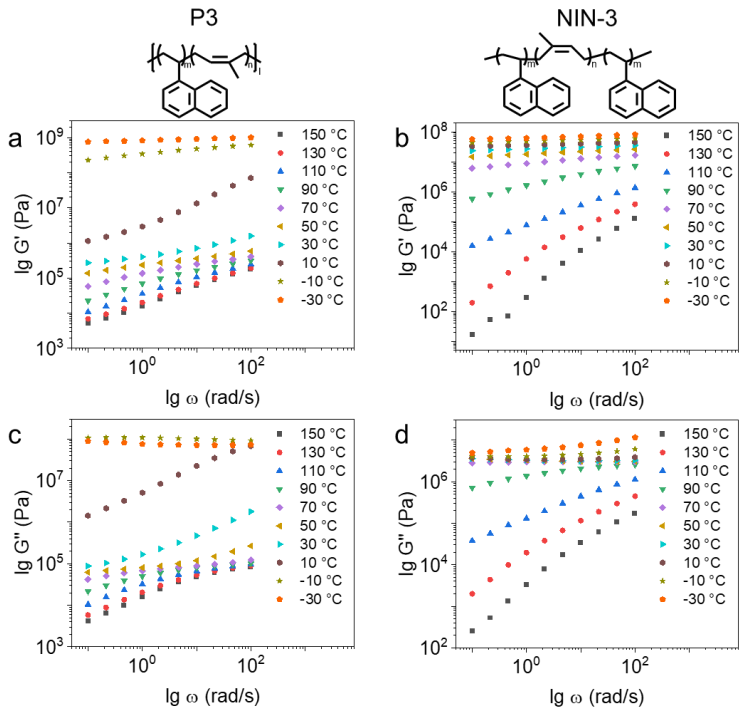

Supplementary Fig. 14. Rheological measurement curves of PNI copolymer and segmented copolymer. Rheological measurement curves: Storage modulus of **a**) P3, **b**) segmented copolymer of NIN-3. Loss modulus of **c**) P3, **d**) NIN-3.

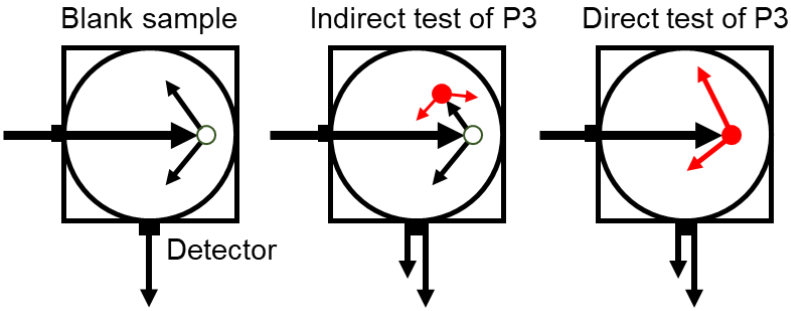

Supplementary Fig. 15. Schematic diagram of the test principle. Measurement of quantum yield of P3 film using the integrating sphere.

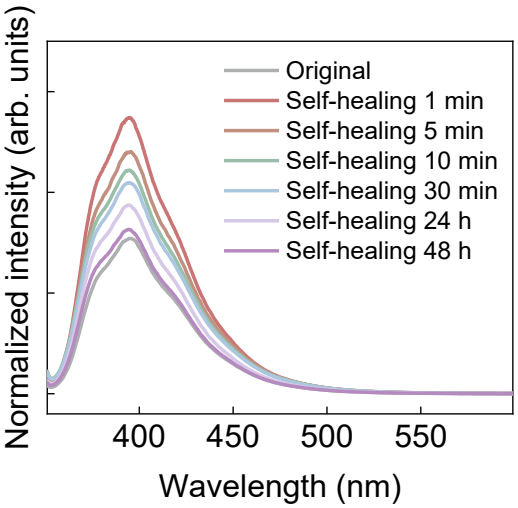

Supplementary Fig. 16. Fluorescence test of copolymer. The fluorescence intensity variation of P3 during self-healing process.

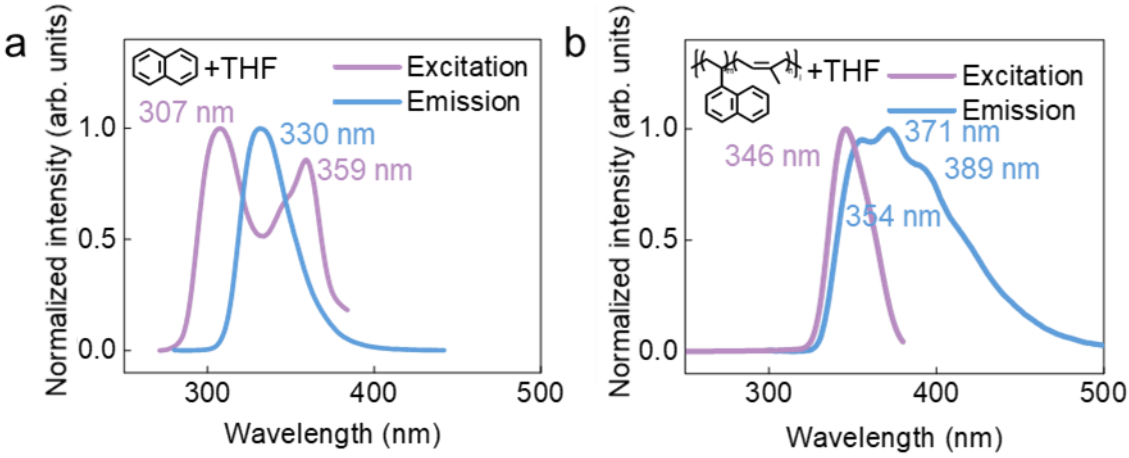

Supplementary Fig. 17. Fluorescent spectra of Naphthalene and PNI copolymer dissolved in THF. **a**) Naphthalene dissolved in THF (1 mM). **b**) P3 dispersed in THF (20 g/L).

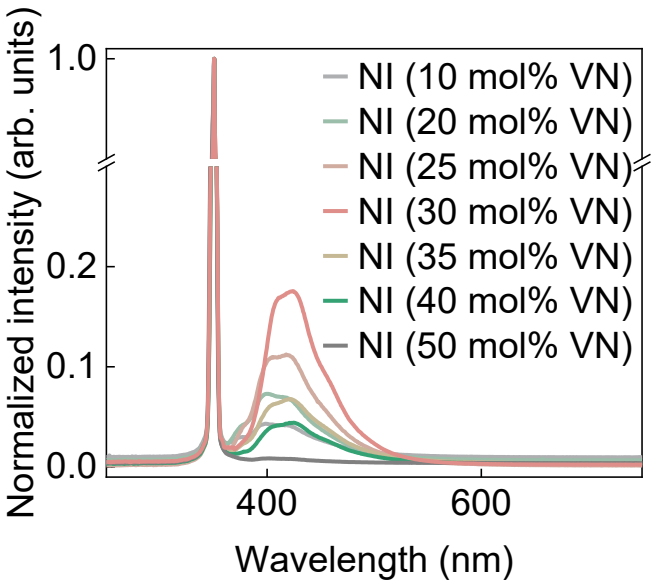

Supplementary Fig. 18. Fluorescence test of copolymer. Fluorescent emission spectra of PNI copolymer with different content of VN (10, 20, 25, 30, 35, 40, and 50 mol%).

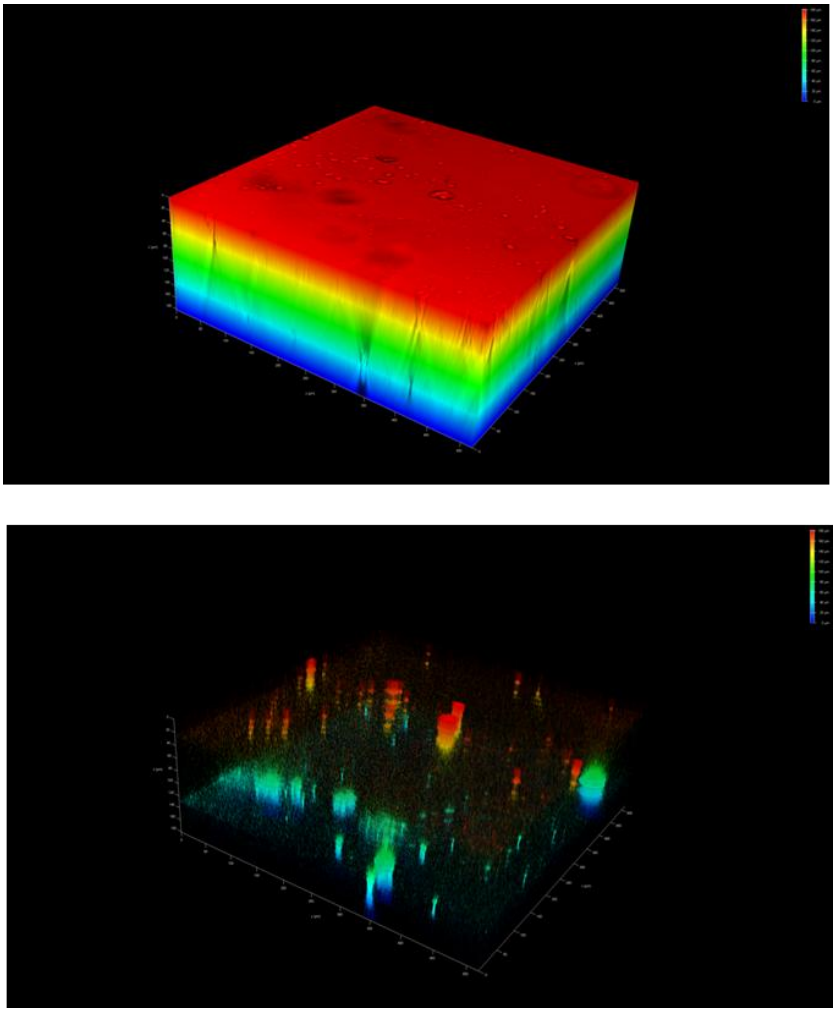

Supplementary Fig. 19. Fluorescent confocal test of copolymer. The 3D reconstruction of P3 block by Z-stack scan of the fluorescent confocal microscope.

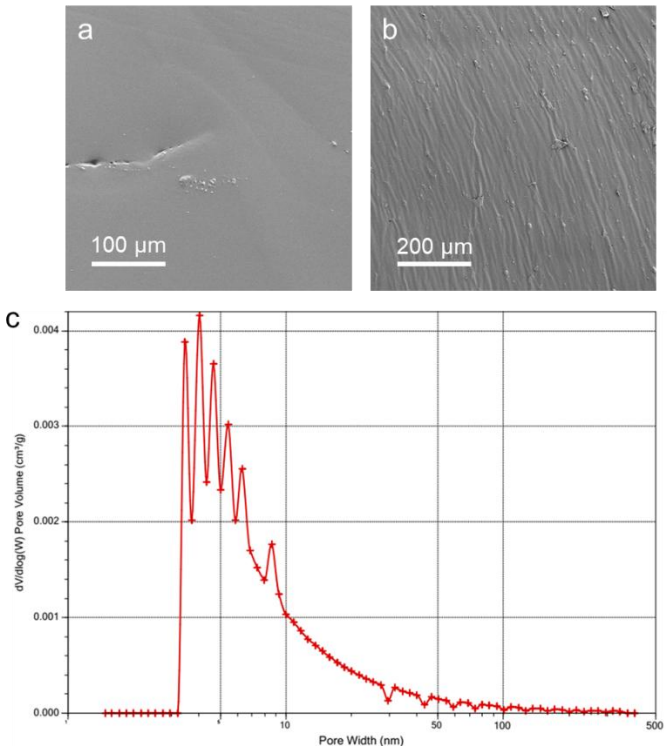

Supplementary Fig. 20. Scanning electron microscope (SEM) images and BET test result of P3. **a**) and **b**) Scanning electron microscope (SEM) images of P3. **c**) Pore size distribution curve of P3 gained by Brunauer-Emmett-Teller test (BET Surface Area: 0.4417 m^2/g).

Supplementary references

1. IUPAC, Compendium of chemical terminology, in: (the "Gold Book"). Compiled by A. D. McNaught and A. Wilkinson, second ed., Blackwell Scientific Publications, Oxford, 1997 https://doi.org/10.1351/goldbook. Online version (2019-) created by S. J. Chalk. ISBN 0-9678550-9-8.

2. J.-C. Bünzli, S.V. Eliseeva, Basics of lanthanide photophysics, springer series on fluorescence, in: P. Hänninen, H. Härmä (Eds.), Lanthanide Luminescence: Photophysical, Analytical and Biological Aspects, vol. 7,

Springer-Verlag Berlin Heidelberg, 2011, ISBN 978-3-642-21022-8 (Chapter 2).

3. Wong, K.-L., Bünzli, J.-C. G. & Tanner, P. A. Quantum yield and brightness. *J. Lumin.* **224**, 117256 (2020).

4. Fries, F.; Reineke, S., Statistical treatment of Photoluminescence Quantum Yield Measurements. *Sci. Rep.* **9** (1), 15638 (2019).